



Ni-nanoclusters hybridized 1T-Mn-VTe₂ mesoporous nanosheets for ultra-low potential water splitting

Uday Narayan Pan^a, Dasu Ram Paudel^a, Amit Kumar Das^a, Thangjam Ibomcha Singh^a, Nam Hoon Kim^{a,*,**}, Joong Hee Lee^{a,b,*}

^a Department of Nano Convergence Engineering (BK21 Four), Jeonbuk National University, Jeonju, Jeonbuk 54896, Republic of Korea

^b Carbon Composite Research Centre, Department of Polymer-Nano Science and Technology, Jeonbuk National University, Jeonju, Jeonbuk 54896, Republic of Korea

ARTICLE INFO

Keywords:

Overall water splitting
Ni-nanoclusters
Vanadium ditelluride
Doping and intercalation
Ultra-low potential
Hybridization

ABSTRACT

Metallic (1T) transition metal dichalcogenides (TMDCs) shows great potential for electrocatalytic water-splitting (ECWS). Among different 1T-TMDCs, vanadium (V)-based 1T-TMDCs has highest thermodynamic stability. Now, among different V-based 1T-TMDCs, 1T-VTe₂ holds the best potential for ECWS due to strongest interlayer coupling between V and Te. In the present study, we have developed nickel nanoclusters (NiNCs) hybridized and manganese (Mn) intercalated and doped 1T-VTe₂ nanosheets (NiNCs-1T-Mn-VTe₂ NS) for ultra-low potential ECWS. Mn doping and intercalation in 1T-VTe₂ (1T-Mn-VTe₂) significantly improve ECWS efficacy following improving oxygen evolution reaction (OER) and hydrogen evolution reaction (HER) performances. Hybridization of NiNCs with 1T-Mn-VTe₂ develop a true ECWS-catalyst NiNCs-1T-Mn-VTe₂ NS for ultra-low potential water-splitting. NiNCs-1T-Mn-VTe₂ NS showed excellent performance requiring only HER-overpotential of 61 mV to reach 10 mA cm⁻² and OER overpotential of 258 mV to reach 40 mA cm⁻². NiNCs-1T-Mn-VTe₂NS (+ -) device required a cell potential of 1.51 V to reach 10 mA cm⁻².

1. Introduction

The growing consumption of fossil fuels to meet excessive energy demands has created enormous adverse impact on the environment and mankind [1]. The only solution for sustainable economic growth is therefore a clean energy initiative [2]. Considering the enormous difficulties in large-scale battery-based energy storage, electrocatalytic water splitting (ECWS) has become the most lucrative alternative for the conversion of renewable solar and wind energy to portable hydrogen fuel [3,4]. ECWS is specifically a function of the two half-reactions, the hydrogen evolution reaction (HER) and the oxygen evolution reaction (OER). The electro-catalyst plays the most crucial role in the commercial viability of the ECWS by reducing the required activation energy for both HER and OER [5]. Hitherto, noble metals like platinum (Pt) and palladium (Pd) are used as HER-catalyst, while ruthenium (Ru), iridium (Ir), and their oxides are used as OER-catalyst [6]. However, their use is limited, due to the high cost and scarcity of the elements. Therefore, for commercial viability of the ECWS, it is of present significance to find out low-cost and earth-abundant resources with excellent performance [6,

7].

Incidentally, transition metal dichalcogenides (TMDCs) have enticed significant attention as ECWS-catalyst, owing to their brilliant mechanical and chemical stability, high abundance in the Earth's crust, intrinsic semiconducting or metallic nature, and high catalytic efficiency [5,6]. TMDCs exhibits layered structures, where the central metal atom (M) stays sandwiched between two chalcogen (C) atoms to develop C-M-C triple atomic planes [5,8]. Following the difference in arrangements of the chalcogen atom in the C-M-C triple atomic planes, the 2D lamellar structures of TMDCs possess polymorphism. They exhibit two discrete crystal phases having entirely dissimilar electronic structures: semiconducting 2H-phase, and metallic 1T-phase [9,10]. Although the 1T-phase of TMDCs shows extraordinary electronic conductivity and accelerates the charge transport reaction in the electrode-electrolyte interface, their low thermodynamical stability possesses significant challenges for repetitive use as catalyst [7,8]. Among different TMDCs, molybdenum (Mo)- or tungsten (W)-based TMDCs predominantly exhibited stable semiconducting 2H-phase, whereas vanadium (V)-based TMDCs exhibited relatively stable metallic 1T-phase [11].

* Corresponding author at: Department of Nano Convergence Engineering (BK21 Four), Jeonbuk National University, Jeonju, Jeonbuk 54896, Republic of Korea.

** Corresponding author.

E-mail addresses: nhk@jbnu.ac.kr (N.H. Kim), jhl@jbnu.ac.kr (J.H. Lee).

<https://doi.org/10.1016/j.apcatb.2021.120780>

Received 31 July 2021; Received in revised form 16 September 2021; Accepted 27 September 2021

Available online 30 September 2021

0926-3373/© 2021 Elsevier B.V. All rights reserved.

Due to this better thermodynamic stability of the highly conductive metallic 1T-phase of VS₂- and VSe₂-based materials, they have been extensively investigated as HER-catalyst, compared to 1T-Mo- or 1T-W-based TMDCs [12]. However, significant challenges regarding the long-term stability during the prolonged reaction were also observed in the case of 1T-VS₂- or VSe₂- based catalysts [13]. Many reports in the literature have investigated that metals ion like Li/K/Mn act as an electron donor to the host phase, hence their presence in the crystals itself, and in the interlayers also, meaningfully enhances the thermodynamic stability of the 1 T-phase of TMDCs [8]. Mn, compared to other metals, has more propensity for stabilizing the 1T-phase of vanadium-based TMDCs, as it shows stable crystal formation in wurtzite, rock salt, or zincblende structures with chalcogen elements, and also forms antiferromagnetic coupling with adjacent chalcogen atom when present in the defect positions [14]. On the other hand, the presence of Mn also has the potential of developing OER-catalytic sites in the vanadium-based TMDCs, which otherwise remains inactive for the OER-catalysis reaction [9,15]. Thus, Mn-intercalation and doping may convert OER-inactive vanadium-based TMDCs to a bifunction ECWS-catalyst, as well as improve the thermodynamic stability of the 1T-phase.

Another interesting class of nanomaterial called metal nanoclusters has emerged as superior electrocatalysts compared to their nanoparticles, due to their high surface area, unique atomic arrangement, and low hydrogen adsorption free energy [16,17]. Compared to other earth abundant metal nanoclusters, Nickel nanoclusters (NiNCs) showed the best performance for HER, OER, and oxygen reduction reaction (ORR) [18,19]. Hence, to improve the catalytic efficacy of vanadium-TMDC-based nanomaterials for low potential water splitting, hybridization of them with NiNCs could be an ideal direction [19]. To date, different VS₂- or VSe₂-based nanomaterials have been investigated for ECWS, but to the best of our knowledge, vanadium ditelluride (VTe₂)-based materials have never been investigated for it [11,12]. Recent understanding of the different intrinsic electronic properties of metallic VTe₂ showed that it holds more potential for ECWS than VS₂ or VSe₂ [20]. Specifically, the interlayer coupling between vanadium and telluride in metallic VTe₂ is much stronger than the other chalcogens counterparts, i.e., sulfide or selenide, making metallic VTe₂ much more stable, compared to the metallic VS₂ or VSe₂ [13]. Moreover, due to the formation of charge density wave (CDW) in metallic VTe₂, substantial charge transfer occurs between the Te (p) and V (d) bands via the Te p_z orbitals, making 1T-VTe₂ much more suitable for fast charge transfer reaction [20]. Furthermore, Mn doping in the interlayers or in interstitial positions of VTe₂ could also have significant influence to arrange the Te-V-Te triple atomic planes toward 1T-fashion like other TMDCs as discussed before, hence, could improve the stability to 1T-VTe₂ significantly [13]. Herein, we have developed NiNCs-hybridized metallic 1T-Mn-VTe₂ mesoporous nanosheets (NiNCs-1T-Mn-VTe₂ NS) for ultra-low potential water splitting. In this report, the hybridization of transition metal nanoclusters with TMDCs is carried out for the first time; moreover, this is the first report regarding metallic 1T-VTe₂-based nanomaterials for bifunctional superior electrocatalytic overall water splitting. Doping and intercalation of the Mn increases the stability of the metallic 1T-phase of the VTe₂, introducing OER catalytic activity along with the development of superior nanosheet structures with high surface area and porosity. NiNCs itself has very high efficacy for water splitting, thus hybridization of NiNCs with 1T-Mn-VTe₂ helps in the development of a super-high-efficient bifunctional electrocatalyst for ultra-low-potential water splitting.

2. Experimental details

2.1. Chemicals

Nickel foam (Ni-foam) with pore size (0.2 – 0.5) mm and thickness ~1.5 mm was purchased from Taiyuan Liyuan Lithium Technology Co.

Ltd., China. Ammonium metavanadate (NH₄VO₃), nickel (II) acetate tetrahydrate [Ni (OCOCH₃)₂·4H₂O], manganese (II) acetate (Mn (CH₃CO₂)₂), Ammonium hydroxide solution (NH₄OH, 28% NH₃ in H₂O), Glutathione (GSH), Sodium borohydride (NaBH₄), Chromium(II) acetate, dimer monohydrate [(CH₃CO₂)₂Cr·H₂O]₂, Iron(III) chloride hexahydrate (FeCl₃·6H₂O), Potassium tellurite (K₂TeO₃), urea (CO(NH₂)₂), Hydrazine monohydrate (N₂H₄·H₂O), and Ammonium fluoride (NH₄F) were purchased from Sigma-Aldrich. The purchased chemicals were used without any further purification, and DI water was used as a solvent in all the experiments.

2.2. Materials synthesis

2.2.1. Synthesis of nickel nanoclusters (NiNCs) hybridized 1T-Mn-VTe₂ nanosheets (NiNCs-1T-Mn-VTe₂ NS)

NiNCs-1T-Mn-VTe₂ NS was synthesized in a three stepped process. In the first step, glutathione (GSH) stabilized nickel nanoclusters (NiNCs) were synthesized using size-focusing method developed for gold nanoclusters and NiNCs with some modifications [16,21,22]. In the second step, NiNCs-hybridized Mn-V-layered double hydroxide on Ni-foam was synthesized using the as-synthesized NiNCs and following conventional hydrothermal method [23,24] where Mn and V salts were used as their precursor and NH₄F and urea were used to develop the layered double hydroxides. As during the formation of the Mn-V-layered double hydroxide the NiNCs, does present in the reaction mixture, thus, Mn-V-layered double hydroxides encapsulate the NiNCs within it to produce NiNCs-hybridized Mn-V-layered double hydroxides [22]. In the third step, the NiNCs-hybridized Mn-V-layered double hydroxides were converted to the corresponding telluride (nickel nanoclusters hybridized 1T-Mn-VTe₂) following hydrothermal based tellurization process [25, 26]. The specifics of each step along with promotion mechanism is described below.

2.2.1.1. Synthesis of glutathione (GSH) stabilized nickel nanoclusters (NiNCs).

As mentioned before, glutathione (GSH) stabilized NiNCs was prepared using previously reported size-focusing method established for gold and nickel nanoclusters with slight modifications [16,21,22]. For this initially, 0.25 mmol of nickel (II) acetate tetrahydrate and 2.0 mmol of glutathione (GSH) were mixed with 25 mL water in a round bottom flask, and the reaction mixture was stirred at ice bath (0 °C) for 30 min for allowing the interaction between GSH and nickel (II) salt complete [16]. Then a separate solution was prepared by dissolving 4 mmol of NaBH₄ (151.32 mg) in 5 mL ice-cold water (0 °C). The ice-cold water was prepared by keeping the water in a test tube and the test tube was preserved in an ice bath for 15 min initially. After that, the NaBH₄ powder was directly added to the test tube and sonication was carried out for 1 min in a bath ultrasonicator to dissolve the NaBH₄. The bath ultrasonicator was filled with 40% ice and 60% cold water just before the sonication to keep the temperature of the bath low (0 °C). Finally, after dissolving NaBH₄, the test tube was again kept in the ice bath for 10 min before use. This ice-cold NaBH₄ solution was then added to the previous solution of nickel (II) acetate tetrahydrate and glutathione (GSH) which was in stirring for 30 min in ice bath (0 °C). After the addition of the NaBH₄ the color of the solution was changed to pale brown from pale green for the formation of the nickel-glutathione (Ni-GSH) complex following reduction of the Ni²⁺ to Ni⁰ and the stirring in ice bath was kept continuing for another 20 min for the complete formation of the Ni-GSH complex [16,21]. Following that, the reaction mixture was taken out from the ice bath and kept in water bath of room temperature for 20 min to reach the reaction mixture temperature to room temperature. Then the wall of the round bottom flask wiped with tissue paper and then placed in an oil bath kept preheated at 80 °C. Then the heating of the reaction mixture at 80 °C was continued for 20 min under reflux condition to complete the formation of the NiNCs [16,19]. After that, the heating was stopped, and the reaction mixture was

immediately taken out from the oil bath and allowed to cool to room temperature in open air. After the completion of the reaction the formation of the NiNCs indicated by the change of the color from pale brown to dark brown [16]. In this reaction, nickel (II) acetate tetrahydrate was used as the limiting reagent such that after the completion of the reaction, no additional nickel salt is left, whose presence could otherwise have the propensity to take part or interfere the subsequent synthesis steps. This reaction mixture after synthesis of the NiNCs is termed as “reaction mixture-1” here.

2.2.1.2. Synthesis of NiNCs-hybridized Mn-V-layered double hydroxide (NiNCs-Mn-V-LDH). NiNCs-Mn-V-LDH on Ni-foam was synthesized using the as-synthesized NiNCs as hybridizable NiNCs with Mn-V-LDH and a conventional hydrothermal based synthesis method was followed using NH_4VO_3 and $\text{Mn}(\text{CH}_3\text{CO}_2)_2$ as the precursor salt for V and Mn respectively and NH_4F and urea were used to develop the layered double hydroxides [23,24,27]. Specifically, a solution of 1 mmol ammonium metavanadate (NH_4VO_3) and 0.3 mmol manganese (II) acetate ($\text{Mn}(\text{CH}_3\text{CO}_2)_2$) in 10 mL water was added to the cooled “reaction mixture-1”. Then, 12 mmol of urea and 6 mmol of NH_4F dissolved in 10 mL of water, and this solution was also added to the same reaction mixture. The reaction mixture was then transferred to a Teflon-lined autoclave along with a glass-supported clean Ni-foam of size $5\text{ cm} \times 2\text{ cm}$. The autoclave was then closed, and the reaction mixture was incubated at $\sim 120^\circ\text{C}$ for 12 h. After completion of the reaction, NiNCs-hybridized Mn-V-layered double hydroxide was formed over the Ni-foam. As NiNCs present in the reaction mixture prior to formation of the Mn-V-LDH, thus, during the formation of Mn-V-LDH, it encapsulate the NiNCs within itself to produce NiNCs-hybridized Mn-V-layered double hydroxides [28,29]. Which could also be facilitated by strong interaction of the GSH present on the surface of the NiNCs with the V and Mn ions [17,21]. Moreover, as mentioned before [$\text{Ni}(\text{OCOCH}_3)_2 \cdot 4\text{H}_2\text{O}$] was used as the limiting agent for the synthesis of NiNCs, it also largely eliminate the possibility of any Ni- double layered double hydroxide formation. After the formation of the NiNCs-Mn-V-LDH on Ni-foam, the Ni-foam was then taken out and washed with water and ethanol mixture, and dried at 60°C for 12 h in a vacuumed oven.

2.2.1.3. Tellurization of NiNCs-Mn-V-LDH to prepare NiNCs hybridized 1T-Mn-VTe₂ (NiNCs-1T-Mn-VTe₂ NS). The NiNCs-hybridized Mn-V-layered double hydroxides on Ni-foam was then immersed in a 50 mL solution containing 200 mg of K_2TeO_3 and 3 mL of $\text{N}_2\text{H}_4 \cdot \text{H}_2\text{O}$. The tellurization process was done at $\sim 180^\circ\text{C}$ for 2 h in similar hydrothermal process. The tellurization method followed here is similar to the many earlier report with slight modification in process [25,26,30]. Finally, after completion of the tellurization, the Ni-foam was washed with water and ethanol mixture, and dried at 60°C for 24 h in a vacuumed oven.

2.2.2. Synthesis of the control materials

1 T-Mn-VTe₂ was synthesized by a similar method. Specifically, a solution of 1 mmol ammonium metavanadate and 0.3 mmol of manganese (II) acetate in 10 mL water was added to another solution containing 12 mmol of urea and 6 mmol of NH_4F in 10 mL of water. Then, 30 mL of additional water was added to it, and the reaction mixture was stirred for 30 min. Next, the reaction mixture was similarly transferred to a Teflon-lined autoclave along with a glass supported clean Ni-foam of size $5\text{ cm} \times 2\text{ cm}$. The reaction mixture was then incubated at $\sim 120^\circ\text{C}$ for 12 h in autoclave. Similarly, after completion of the reaction Mn-V-layered double hydroxides was formed over the Ni-foam, and the Ni-foam was washed with water and ethanol mixture, and dried at 60°C for 12 h in a vacuumed oven.

The Mn-V-layered double hydroxides was then similarly immersed in a 50 mL solution containing 200 mg of K_2TeO_3 and 3 mL of $\text{N}_2\text{H}_4 \cdot \text{H}_2\text{O}$. The tellurization process was carried out at $\sim 180^\circ\text{C}$ for 2 h in hydrothermal condition as reported in many previous articles [25,26,30].

Finally, after completion of the tellurization, the samples were washed with water and ethanol mixture, and dried at 60°C for 24 h in a vacuumed oven.

For the synthesis of the other control manganese vanadium tellurides, namely Mn-VTe₂ (1:1), Mn-VTe₂ (1:3), Mn-VTe₂ (4:1), the reaction procedure was kept exactly the same, and only the precursor salt ratio was varied. For Mn-VTe₂ (1:1), 0.65 mmol of manganese (II) acetate and 0.65 mmol of ammonium metavanadate were used, and for Mn-VTe₂ (1:3), 0.3 mmol of ammonium metavanadate and 1 mmol of manganese (II) acetate were used and for Mn-VTe₂ (4:1) 1.04 mmol of ammonium metavanadate and 0.26 mmol of manganese (II) acetate were used. The amounts of NH_4F and $\text{CO}(\text{NH}_2)_2$ were kept the same. The layered double hydroxides were prepared at $\sim 120^\circ\text{C}$ for 12 h in hydrothermal condition, and after that, the similar tellurization process was carried out in similar manner at 180°C [23–27,30]. NiNCs-Mn-VTe₂ (1:3) and NiNCs-Mn-VTe₂ (1:1) was prepared using these molar ratios of precursors and using the same procedure to that of NiNCs-Mn-VTe₂ synthesis.

NiNCs hybridized 1T-VTe₂ (NiNCs-1T-VTe₂) was prepared using the similar procedure to that of NiNCs-1T-Mn-VTe₂ synthesis. For that, first NiNCs was prepared using the same procedure as mentioned before. Then, NiNCs-V-LDH was prepared using this NiNCs and following the process mentioned before. Specifically, a solution of 1.3 mmol ammonium metavanadate (NH_4VO_3) in 10 mL water was added to the NiNCs solution and then, 12 mmol of urea and 6 mmol of NH_4F dissolved in 10 mL of water was again added to this solution. The reaction mixture was then transferred to a Teflon-lined autoclave along with a glass-supported clean Ni-foam of size $5\text{ cm} \times 2\text{ cm}$. The autoclave was then closed, and the reaction mixture was incubated at $\sim 120^\circ\text{C}$ for 12 h. After completion of the reaction, it was allowed to cool down to room temperature (25°C). The prepared NiNCs-V-LDH was then collected and wash with DI water and ethanol and dried in vacuumed oven. This was then converted to the NiNCs-1T-Mn-VTe₂ using same tellurization process mentioned before [25,26,30].

Manganese doped 1T-VTe₂ (Mn-1T-VTe₂), chromium doped VTe₂ (Cr-VTe₂) and iron doped VTe₂ (Fe-VTe₂) were also synthesized using the same procedure used to synthesized Mn-VTe₂ (1:1) as mentioned before. First, the desired LDHs were synthesized and then these LDH were converted to their corresponding tellurides. For Mn-V-LDH, 1 mmol ammonium metavanadate (NH_4VO_3) and 0.3 mmol manganese (II) acetate ($\text{Mn}(\text{CH}_3\text{CO}_2)_2$) were used, and for Cr-V-LDH, 1 mmol ammonium metavanadate (NH_4VO_3) and 0.3 mmol chromium(II) acetate, dimer monohydrate [$(\text{CH}_3\text{CO}_2)_2\text{Cr} \cdot \text{H}_2\text{O}$]₂ were used and for Fe-V-LDH 1 mmol ammonium metavanadate (NH_4VO_3) and 0.3 mmol iron(III) chloride hexahydrate ($\text{FeCl}_3 \cdot 6\text{H}_2\text{O}$) were used. Then, these LDHs were converted to the respective telluride using the same tellurization process described before [25,26,30].

2.2.3. Preparation of Pt/C and RuO₂ electrode

Platinum on carbon (Pt/C, 10 wt%) ink was prepared by dispersing 10 mg of Pt/C using 950 μL of isopropyl alcohol and 50 μL nafion (5 wt %), following sonication for 30 min. The ink was then drop casted on a $1\text{ cm} \times 1\text{ cm}$ Ni-foam, and then dried entirely in an oven at 60°C . RuO₂ ink was also prepared in similar manner. Specifically, first, 10 mg of ruthenium (IV) oxide was mixed with 950 μL of isopropyl alcohol and 50 μL of 5% nafion solution. Then the mixture was sonicated for 30 min to prepare the ink. Next, the RuO₂ ink was coated on $1\text{ cm} \times 1\text{ cm}$ clean Ni-foam, and dried out [31,32].

2.3. Physical characterizations

Field emission scanning electron microscopy (Maker: Supra 40 VP instrument Zeiss Co., Germany) and transmission electron microscopy (Maker: JEM-2200FS instrument JEOL Co., USA) were used for the morphological characterization. X-ray diffraction meter (Maker: D/Max 2500 V/PC; Rigaku Co., Japan) was used for crystallographic

characterization at the Center for University-Wide Research Facilities (CURF), Jeonbuk National University (Korea). Cu target K α X-ray ($\lambda = 0.154$ nm) was used as the source for the X-ray. X-ray photoelectron spectrometry (Maker: VG ESCALAB 220i, Thermo Fisher, UK) in the Jeonju center of KBSI and Raman spectrometry (Maker: Nanofinder 30, Tokyo Instruments, INC., Japan) were used to obtain spectroscopic data. Raman data was obtained using 532 nm laser excitation with laser power of 0.2 mW.

2.4. Electrochemical characterization

Electrochemical workstation (Maker: CHI660E CH Instruments, Inc., USA) was used for all the electrochemical measurements. Graphite rod was used as counter electrode. Saturated Ag/AgCl electrode (3.0 mol L⁻¹ KCl) was used as the reference electrode. The same electrochemical workstation was used for electrochemical impedance spectroscopy (EIS) with 5 mV amplitude AC voltage having a frequency range of (0.01 Hz to 100 kHz). Electrochemical surface area (ECSA) was also measured using the same workstation in non-faradic regions at varying scan rates from (10–100) mV s⁻¹ [31,32]. For all the as-synthesized catalysts (grown on Ni-foam) or commercial Pt/C and RuO₂ catalysts (drop casted on Ni-foam), a size 1 cm × 1 cm electrode was used as working electrode to measure their HER, OER and overall water-splitting performance. The mass loading on 1 cm × 1 cm electrode of NiNCs-1T-Mn-VTe₂ NS catalyst was found to be ~3.46 mg. For commercial Pt/C and RuO₂ catalysts, a similar mass loading on 1 cm × 1 cm size Ni-foam was used. Experimentally, the mass loading for Pt/C and RuO₂ was found to be ~3.48 mg and ~3.45 mg respectively on 1 cm × 1 cm size Ni-foam [33].

2.5. Calculations

$$E_{(vs-RHE)} = E_{(vs-AgCl)} + 0.0591 \text{ pH} + E_{Ag/AgCl}^{\circ} \quad (1)$$

Eq. (1) was used to convert the experimentally measured potential to reversible hydrogen electrode potential ($E_{(vs. RHE)}$) [34].

$$E_{IR-corrected} = E_{(vs-RHE)} - I \times R_s \quad (2)$$

Eq. (2) was used to obtain the IR-corrected potential, where 'I' is the current, and 'R_s' is the equivalent series resistance [31,32].

$$\eta = a + b \log j \quad (3)$$

Eq. (3) was used to obtain the Tafel slope, where ' η ' is the over-potential, ' b ' is the Tafel slope, ' j ' is the current density, and ' a ' is a constant [31,32].

$$ECSA = \frac{C_{dl}}{C_s} \quad (4)$$

Eq. (4) was used to calculate the electrochemically active surface area (ECSA), where 'C_s' is the specific capacitance of a flat surface, and 'C_{dl}' is the double-layer capacitance [31,32]. C_{dl} was evaluated by recording cyclic voltametric (CV) profiles in a non-Faradaic potential region of 1.125–1.225 V at multiple scan rates [31].

$$\text{Faradaic efficiency (FE)} = \frac{N_{\text{measured}}}{J \cdot t / nF} \quad (5)$$

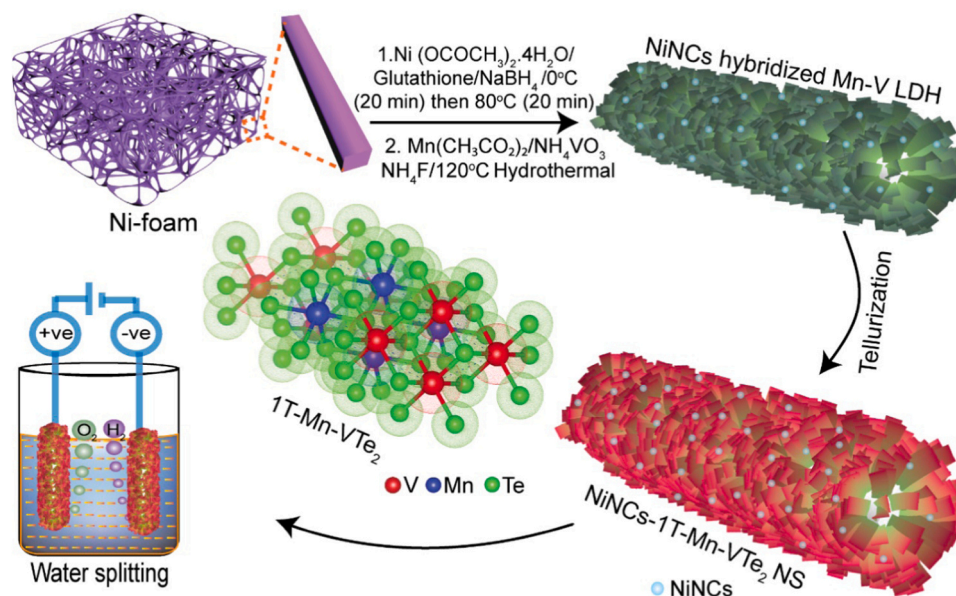
Eq. (5) is used to measure the Faradaic efficiency, where, N_{measured} representing the amount of measured O₂ or H₂ gas (unit: mol), J is the constant oxidation/reduction current density (unit: mA cm⁻²) used, t is the total electrolysis time (unit: second), n represents electron transfer number, and F represents Faraday constant (96485 Cmol⁻¹) [34].

3. Results and discussion

3.1. Synthesis and structural characterization

The nickel nanoclusters (NiNCs) hybridized 1T-Mn-VTe₂ nanosheets (NiNCs-1T-Mn-VTe₂ NS) was prepared in a three-stepped reaction. First, NiNCs were synthesized and then the NiNCs-hybridized Mn-V-layered double hydroxides (NiNCs-Mn-V-LDH) was prepared using those NiNCs, and in the 3rd step, tellurization of NiNCs-Mn-V-LDH was carried out to prepare Ni-nanoclusters-hybridized 1T-Mn-VTe₂ (NiNCs-1T-Mn-VTe₂ NS; Scheme 1, details may be found in the experimental section). The sample named 1T-Mn-VTe₂ contains V and Mn in 3:1 ratio; three other control samples Mn-VTe₂ (1:3), Mn-VTe₂ (1:1) and Mn-VTe₂ (4:1), where the ratio of V and Mn was kept at 1:3, 1:1, and 4:1 respectively, were also prepared. For all the samples, first, double-layered hydroxides of the respective sample were prepared, and then the tellurization was carried out (details may be found in the experimental section).

The elemental compositions of all the samples were confirmed using inductively coupled plasma-optical emission spectrometry (ICP-OES) and atomic absorption spectrometry (AAS, Table S1, Supporting information). The elemental composition is found to be similar to the precursor ratio of the elements used for the synthesis [5]. The morphological characteristics of all the samples were investigated using field emission scanning electron microscopy (FESEM) imagery. The FESEM images of the NiNCs-1T-Mn-VTe₂ NS (Fig. 1A–C) show clear ultrathin nanosheet structure. The images also showed that the nanosheets are highly uniform, and interconnected with one another. The average thickness of the sheets was calculated to be ~2 nm using the FESEM images. Fig. S1 of the Supporting information shows the FESEM images of the control samples i.e., 1T-Mn-VTe₂, Mn-VTe₂ (1:3), and Mn-VTe₂ (1:1). The results show that the sheet structure of the 1T-Mn-VTe₂ is similar to NiNCs-1T-Mn-VTe₂ NS, indicating no significant changes in the basic morphology of the material following hybridization with the NiNCs (Fig. S1A–C, Supporting information). The Mn-VTe₂ (1:3) and Mn-VTe₂ (1:1) showed highly irregular morphology, where sheet structures were neither grown precisely, nor uniformly (Fig. S1D–I, Supporting information). The FESEM images of Mn-VTe₂ (4:1) and 1T-VTe₂ also showed the growth of the sheet structure but the sheets are smaller in size and much less organized (Fig. S2, Supporting information). Thus, the FESEM results showed the importance of Mn-doping for improving the morphology and also indicated that the 3:1 ratio of V to Mn is the best ratio for the fabrication of the Mn-V bimetallic telluride with superior sheet structure. The FESEM images of the NiNCs-hybridized Mn-V-layered double hydroxides (NiNCs-Mn-V-LDH, synthesis details may be found in the experimental section) were also obtained (Fig. S3, Supporting information). These images, when compared with the FESEM images of the NiNCs-1T-Mn-VTe₂ NS (Fig. 1A–C) showed no significant changes in the morphology, clearly indicating that the tellurization process does not substantially affect or change the morphology and structure of the NiNCs-Mn-V-LDH. Transmission electron microscopy (TEM) imagery of the NiNCs-1T-Mn-VTe₂ NS was acquired to investigate the morphology and the crystallographic structure of the material (Fig. 1D and E). The sheet structure obtained from the TEM imagery and the FESEM imagery showed resemblance. The TEM imagery also clearly showed the presence of the NiNCs. Some of the NiNCs are highlighted using dotted circles in Fig. 1E for clear understanding. Comparison of the TEM imagery of NiNCs-1T-Mn-VTe₂ NS with 1T-Mn-VTe₂ (Fig. S4, Supporting information) showed that the NiNCs-1T-Mn-VTe₂ NS has clear presence of NiNCs, whereas the 1T-Mn-VTe₂ does not show the presence of any such nanoclusters, thus, confirming the hybridization of the NiNCs with 1T-Mn-VTe₂. The high-resolution transmission electron microscopic (HRTEM) imagery of NiNCs-1T-Mn-VTe₂ NS (Fig. 1F), their corresponding inverse fast Fourier transform (IFFT) images (Fig. 1G₁, H₁, & I₁) and fast Fourier transform (FFT) images (Fig. 1G₂,



Scheme 1. Schematic of the fabrication of the nickel nanoclusters-hybridized 1 T-Mn-VTe₂ nanosheets (NiNCs-1 T-Mn-VTe₂ NS) and its utilization as a superior electrocatalyst for overall water splitting.

H₂, & I₂) show the presence of lattice fringes for both 1T-Mn-VTe₂ and NiNCs, conclusively establishing the formation of the NiNCs-1T-Mn-VTe₂ NS [5–7]. The elemental mapping of the NiNCs-1T-Mn-VTe₂ NS (Fig. 1J) also shows the presence of all the constituent elements, namely V, Ni, Mn, and Te [5]. The mesoporous nature of the 1T-Mn-VTe₂ NS was confirmed by additional low resolution TEM image (Fig. S5A, Supporting information) and high-angle annular dark-field scanning transmission electron microscopy (HAADF-STEM) image (Fig. S5B, Supporting information). Some of the mesopores are marked in yellow (Fig. S5A, Supporting information) and red (Fig. S5B, Supporting information) circles. Specifically, the HAADF-STEM (Fig. S5B, Supporting information) clearly showed the presence of mesopores thus, conclusively proved the formation of the mesoporous architecture of the NiNCs-1T-Mn-VTe₂ [36].

3.2. Surface area, crystallographic and spectroscopic characterizations

Synchronous results with the FESEM images were also observed in the N₂ adsorption–desorption Brunauer–Emmett–Teller (BET) isotherms (Fig. 2A). The results showed that NiNCs-1T-Mn-VTe₂ NS has the highest surface area of 92 m² g^{−1} with an average pore diameter of 24.3 nm (Fig. 2A, and Fig. S6, Supporting information). Mn-VTe₂ (1:3) and Mn-VTe₂ (1:1) exhibited surface area of (69.1 and 56.5) m² g^{−1} with average pore diameter (11.1 and 17.9) nm, respectively (Fig. 2A, and Fig. S6, Supporting information). The other control materials, 1T-VTe₂, NiNCs-1T-VTe₂, 1T-Mn-VTe₂ and Mn-VTe₂ (4:1) exhibited surface area of 45 m² g^{−1}, 51 m² g^{−1}, 83 m² g^{−1} and 64 m² g^{−1} (Fig. S7A, Supporting information) with average pore diameter of 8.3 nm, 7.9 nm, 23.2 nm and 13.5 nm (Fig. S7B, Supporting information) respectively. Thus, we can conclude NiNCs-1T-Mn-VTe₂ displayed better morphology and surface area, compared to the other control materials with mesoporous architecture [5–7]. Basically, layered double hydroxides (LDHs) in most cases itself has porous architecture due to the formation of generic layer sequences and more importantly, when LDHs are subjected to chalcogenization following hydrothermal methods, it creates significant alteration of the crystal alignments, along with the removal of trapped gas molecules (O₂ and N₂) leading to enhancement of the porous constructions substantially, this could be the possible reason for the formation of mesoporous architecture of NiNCs-1T-Mn-VTe₂ [7,23,27,37]. For further crystallographic analysis after HRTEM, powder X-ray

diffraction (PXRD) investigation of NiNCs-1 T-Mn-VTe₂ NS was carried out, and Fig. 2B presents the results. The results showed peaks (2θ) at (14.3, 29.4, 42.2, 58.8, and 69.9)° corresponding to the (001), (002), (003), (004), and (005) planes of 1T-Mn-VTe₂ (powder diffraction files from crystallography open database (PDF-COD) card number 04-007-8849), confirming the formation of the same [11,12,20,38]. Some peaks of relatively low intensity at 2θ = (44.1, 50.4, and 75.2)° were also observed, which correspond to the (111), (002), and (022) planes of NiNCs (PDF-COD card number 96-201-2279) [16,19,39,40].

The relatively low intensity of the NiNCs peaks compared to the 1T-Mn-VTe₂ peaks is attributed to the presence of a comparatively low amount of NiNCs relative to that of 1T-Mn-VTe₂ in NiNCs-1T-Mn-VTe₂ NS, which is observed from the TEM images also (Fig. 1D & E, and Figs. S4,5, Supporting information) [33,35]. PXRD of 1T-VTe₂, 1T-Mn-VTe₂, Mn-VTe₂ (4:1), and NiNCs-1T-VTe₂ was also obtained (Fig. S8, Supporting information). PXRD of 1T-VTe₂ showed peaks corresponding to the (001), (002), (003), (004), and (005) planes matching with PDF-COD card number 04-007-8849 and peaks regarding NiNCs are naturally absent here (Fig. S8A, Supporting information) [11,12,20,38]. 1T-Mn-VTe₂ and Mn-VTe₂ (4:1), (Fig. S8B,C, Supporting information) understandably has a similar PXRD pattern to that of 1T-VTe₂ and also matches with PDF-COD card number 04-007-8849 and no additional NiNCs peak was observed [11,12,20,38]. Whereas, in case of NiNCs-1T-VTe₂, additional NiNCs peaks are observed along with the 1T-VTe₂ peaks (Fig. S8D, Supporting information) and the NiNCs peaks were found to match with the PDF-COD card number 96-201-2279 [16,19,39,40]. Importantly, to find out the nature of the Mn doping, PXRD of NiNCs-1T-Mn-VTe₂ was compared with the PXRD of 1T-VTe₂ (Fig. S9, Supporting information). No significant shift in the position of the peaks regarding 1T-VTe₂ was observed in NiNCs-1T-Mn-VTe₂ indicating the doping of Mn in 1T-Mn-VTe₂ is mostly in interstitial sites and no significant partial substitution of V is occurred [41,42]. However, as for the synthesis of the present NiNCs-1T-Mn-VTe₂ catalyst, a bottom up synthesis process is followed, thus, a significant amount of interlayers doping is also expected along with the interstitial positions doping due to the incapability of bottom up synthesis process regarding controlling the specific doping site [5–7]. Fig. 2C–F plot the X-ray photoelectron spectroscopic (XPS) investigation of NiNCs-1T-Mn-VTe₂ NS was also carried out. The high-resolution XPS (HRXPS) spectra of V 2p showed the presence of peaks at (524.7 and

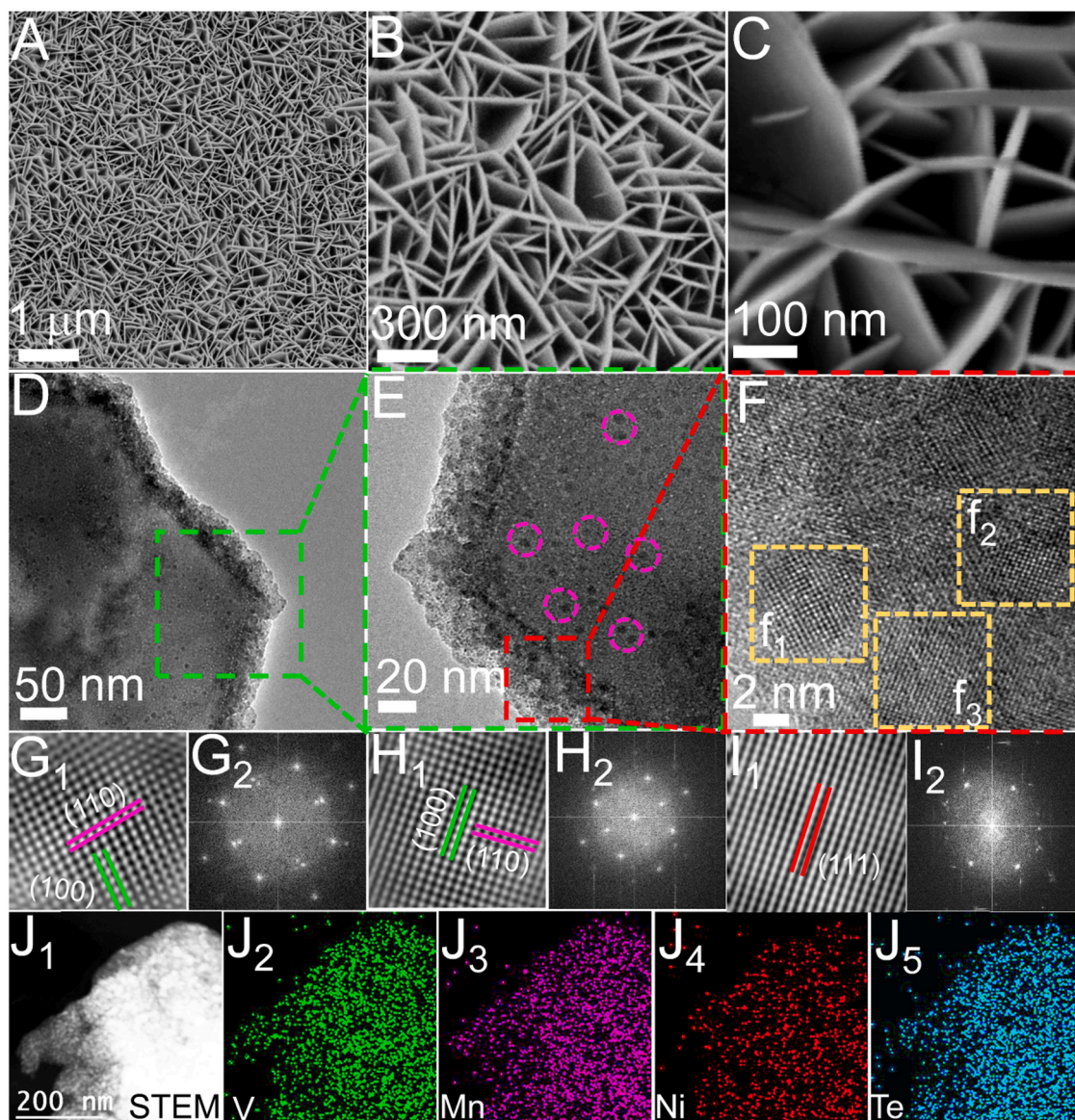


Fig. 1. (A)–(C) FESEM images of the NiNCs–1T–Mn–VTe₂ NS at different magnification. (D) & (E) TEM images of NiNCs–1T–Mn–VTe₂ NS clearly showing the sheet structure and the presence of NiNCs (some are marked in circle). (F) High-resolution transmission electron microscopy (HRTEM) images of NiNCs–1T–Mn–VTe₂ NS; boxes (f₁) and (f₂) are the HRTEM of 1T–Mn–VTe₂, while box (f₃) is the HRTEM of NiNCs. (G₁), (H₁), & (I₁) are the inverse fast Fourier transform (IFFT) of the f₁, f₂, & f₃ areas, respectively. (G₂), (H₂), & (I₂) are the fast Fourier transform (FFT) of the f₁, f₂, & f₃ areas, respectively [5–7] (J) Elemental mapping of the NiNCs–1T–Mn–VTe₂ NS showing the presence of constituent elements: (J₁) scanning transmission electron microscopic (STEM) image of NiNCs–1T–Mn–VTe₂ NS; (J₂) elemental mapping corresponding to vanadium (V); (J₃) elemental mapping corresponding to manganese (Mn); (J₄) elemental mapping corresponding to nickel (Ni); and (J₅) elemental mapping corresponding to tellurium (Te).

517.1 eV corresponding to V 2p_{1/2} and V 2p_{3/2} (Fig. 2C). Deconvolution of the spectrum showed presence of deconvoluted peaks at binding energies of 524.6 eV, 523.3 eV, 517.1 eV and 516.5 eV corresponding to V⁵⁺ 2p_{1/2}, V⁴⁺ 2p_{1/2}, V⁵⁺ 2p_{3/2} and V⁴⁺ 2p_{3/2} respectively (Fig. 2C) [11, 12, 20, 38]. The HRXPS spectrum of Te 3d showed the presence of peaks at (586.6 and 576.3) eV corresponding to TeO₂ (3d_{3/2}) and TeO₂ (3d_{5/2}), respectively (Fig. 2D). HRXPS peaks at (583.1 and 572.7) eV correspond to Te-metallic (3d_{3/2}) and Te-metallic (3d_{5/2}), respectively (Fig. 2D). The presence of TeO₂ (3d_{3/2}) and TeO₂ (3d_{5/2}) peaks are due to aerial surface oxidation of the NiNCs–1T–Mn–VTe₂ NS. Importantly, Te-metallic (3d_{3/2}) and Te-metallic (3d_{5/2}) peaks are well separated spin-orbit components at $\Delta E_{\text{metal}} = 10.4$ eV, conclusively proving the formation of telluride phase [10–13, 43]. Moreover, the nature of the high-resolution V 2p and Te 3d spectra clearly match those of the other reported metallic (1T) vanadium ditelluride-based materials [10–13,

43]. HRXPS spectra of Mn 2p showed the presence of peaks at (653.4, 646.7, and 641.8) eV corresponding to Mn 2p_{1/2}, and Mn 2p_{3/2} (Fig. 2E) [7, 14]. The deconvoluted spectra showed presence of deconvoluted peaks at 655.4 eV, 654.0 eV, 652.6 eV, 646.0 eV, 643.1 eV, and 641.3 eV corresponding to Mn⁴⁺ 2p_{1/2}, Mn³⁺ 2p_{1/2}, Mn²⁺ 2p_{1/2}, Mn⁴⁺ 2p_{3/2}, Mn³⁺ 2p_{3/2} and Mn²⁺ 2p_{3/2} respectively (Fig. 2E) [7, 14]. HRXPS spectrum of Ni 2p showed peaks at (869.1 and 851.3) eV corresponding to Ni 2p_{1/2} and Ni 2p_{3/2}, and their corresponding satellite peaks at binding energies ~ (875.4) and (862.5) eV respectively (Fig. 2F) [7, 14]. Deconvolution of the spectrum showed the presence of dominant deconvoluted peaks at 851.2 eV and 868.8 eV that corresponds to the presence of metallic Ni clusters, while the peaks at 870.7 eV and correspond to Ni²⁺ species respectively (Fig. 2F) [5, 16, 19].

Overall, the XPS analysis confirms the presence of all the constituent elements in their respective oxidation states, and conclusively confirms

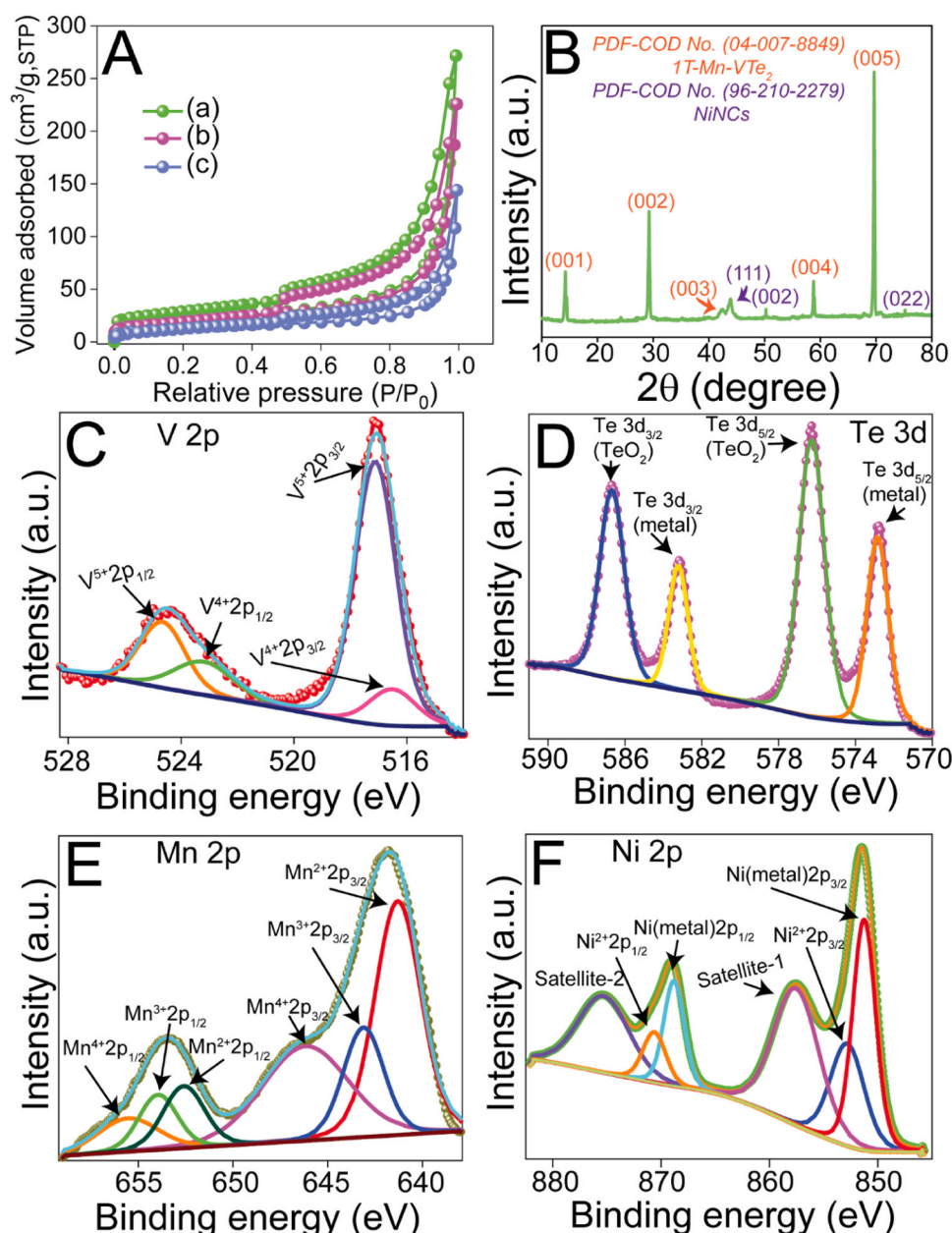


Fig. 2. (A) N₂ adsorption–desorption Brunauer–Emmett–Teller (BET) isotherms of (a) NiNCs–1T–Mn–VTe₂ NS, (b) Mn–VTe₂ (1:3), and (c) Mn–VTe₂ (1:1) (B) Powder X-ray diffraction (PXRD) pattern of NiNCs–1T–Mn–VTe₂ NS. Deconvoluted high-resolution XPS spectra of (C) Vanadium 2p, (D) Tellurium 3d, (E) Manganese 2p, and (F) Nickel 2p for NiNCs–1T–Mn–VTe₂.

the formation of the NiNCs–1T–Mn–VTe₂ NS. It is to be mentioned here that high inherent stability of the NiNCs at magic number of 561–2057 atoms makes NiNCs very stable once synthesized and less prone to disruption by outer environmental changes [44,45] thus, limits the possibility of the oxidation or tellurization of the NiNCs to the nickel oxide or telluride in the subsequent steps of the reaction performed using the NiNCs as starting materials (details regarding reaction steps are in the experimental section). Moreover, GSH acts as a strong capping agent for NiNCs which also limit the surface oxidation and tellurization of the NiNCs during the subsequent reaction [16,19]. However, partial surface oxidation and tellurization of the NiNCs can't be completely overruled during the succeeding hydrothermal reaction considering the presence of dangling bonded Ni layer over NiNCs primary surface [16, 19]. The XPS results here shows the presence of both Ni²⁺ and Ni⁰ in NiNCs–1T–Mn–VTe₂. However, the intensity regarding Ni⁰ peaks are much higher compared to the Ni²⁺ peaks, indicating majority of the Ni

in NiNCs are present in Ni⁰ form, although, presence of Ni²⁺ also indicating that possibly some of the dangling bonded Ni were oxidized or tellurized (Ni²⁺) during the subsequent course of reactions (Fig. 2F) [5, 16,19].

Now, as mentioned before, interlayer coupling between vanadium and telluride in metallic VTe₂ is very strong and it meaningfully enhances the ECWS efficacy of the TMDCs. To examine the extend the interlayer coupling in NiNCs–1T–Mn–VTe₂ NS, photoluminescence spectroscopic investigation is performed (Fig. S10, Supporting information). Strong interlayer coupling creates spatially separated electron–hole pairs inhabiting in different layers in the layered transition metal dichalcogenides (LTMDs) [46,47]. Furthermore, the spatially separated electron–hole pairs can also introduce a permanent electric dipole moment depending upon the extend of the interlayer coupling [46,48]. These formation of electron–hole pairs and permanent electric dipole generates photoluminescence properties in those LTMDs where

interlayer coupling is very strong. Whereas, LTMDs with weak interlayer coupling loosens the lattice matching requirement, hence, separation of electron–hole pairs become difficult and the LTMDs fails to exhibit photoluminescence [46–48]. We observed strong PL emission characteristic in 1T-VTe₂ which itself indicates a strong interlayer coupling phenomenon in 1T-VTe₂ (Fig. S10, Supporting information). Moreover, increase in PL intensity in NiNCs-1T-Mn-VTe₂ compared to 1T-VTe₂ and slight shift of the emission peak towards lower energy region indicates an increase in the extend of interlayer coupling in NiNCs-1T-Mn-VTe₂ than 1T-VTe₂ (Fig. S10, Supporting information) [46–48]. This increase in interlayer coupling could be because of the presence of Mn in the interlayers of 1T-VTe₂ in NiNCs-1T-Mn-VTe₂, as Mn has different electronic properties than V. Thus, 1T-VTe₂ heterobilayers can act as a set of independent monolayers, in Mn doped 1T-VTe₂ thereby, significantly improving the extend of interlayer coupling [46–48].

3.3. Measurements of electrocatalytic performance

The electrochemical performance of all the materials were measured in order to determine their HER and OER catalytic activity. Both HER

and OER are measured in a conventional three-electrode arrangement. N₂-saturated 1 M KOH was used as electrolyte, graphite-rod was used as counter electrode, and saturated Ag/AgCl electrode was used as reference electrode. Different catalysts grown on Ni-foam of size 1 cm × 1 cm were used as working electrode to measure their HER and OER performance [5,31–34,42]. The linear sweep voltammetry (LSV) measurements of all the samples for HER were carried out at the scan rate 2 mV s⁻¹, and the LSV curves after IR-correction that were plotted. The results showed that NiNCs-1T-Mn-VTe₂ NS, 1T-Mn-VTe₂, Mn-VTe₂ (1:3), Mn-VTe₂ (1:1), 1T-VTe₂, and Pt/C required overpotentials (η_{HER}) of (61, 110, 129, 162, 172, and 30) mV to reach the current density of 10 mA cm⁻², and (137, 175, 193, 233, 315, and 50) mV to reach the current density of 50 mA cm⁻², respectively (Fig. 3A & B). The other control materials NiNCs-1T-VTe₂, Mn-VTe₂(4:1), NiNCs-Mn-VTe₂ (1:1), and NiNCs-1T-VTe₂ (1:3) required overpotentials (η_{HER}) of (178, 165, 154, and 121) mV to reach the current density of 10 mA cm⁻², and (258, 236, 208, and 184) mV to reach the current density of 50 mA cm⁻², respectively (Fig. S11A, Supporting information). Bare Ni-foam does not show any significant catalytic activity, and thus, has negligible influence on the measured overpotentials of the different catalysts (Fig. 3A). The results show that NiNCs-1T-Mn-VTe₂ NS has the lowest η_{HER} among the

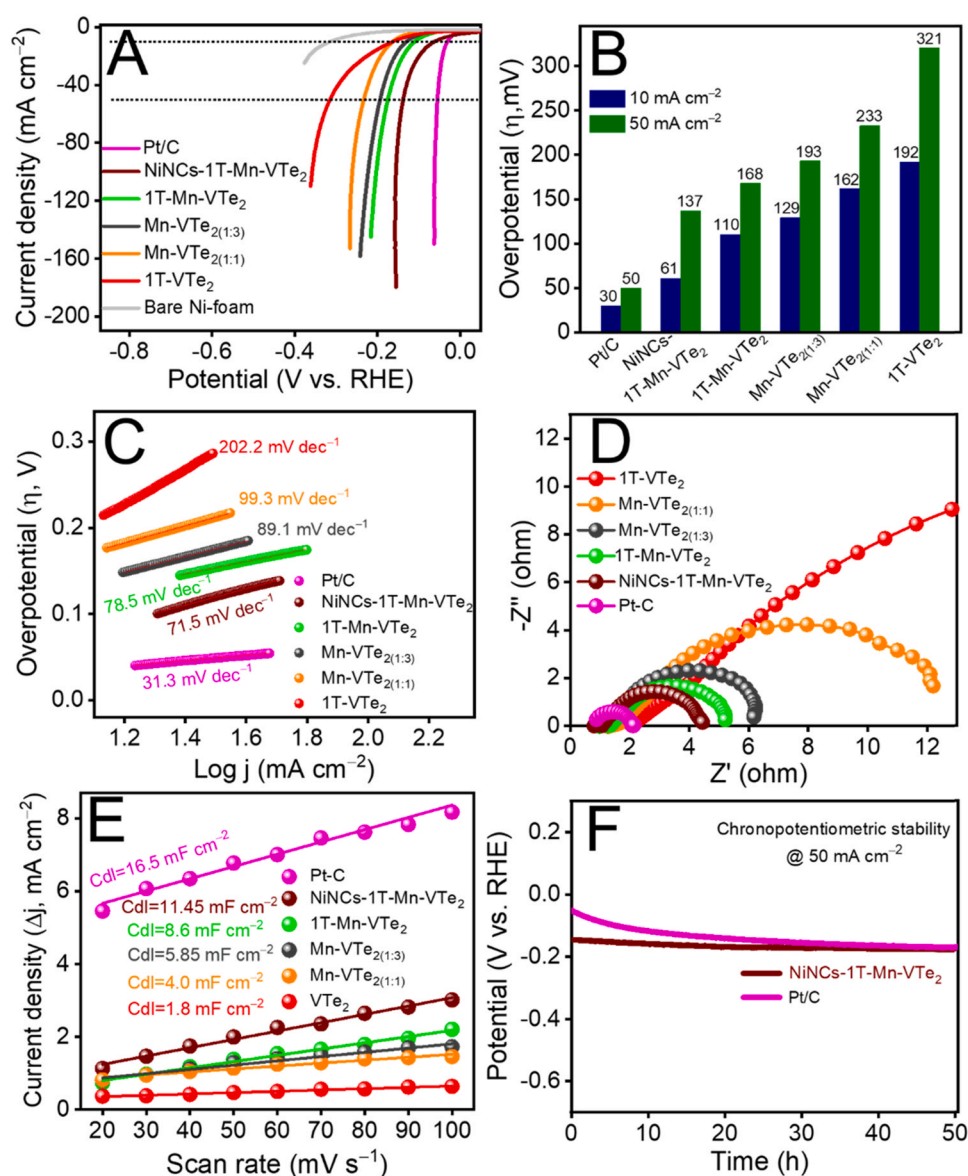
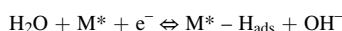


Fig. 3. (A) Linear sweep voltammetry (LSV) measurements curves for the hydrogen evolution reaction (HER) of different materials. (B) Overpotential comparison (HER) of the materials at current densities of (10 and 50) mA cm⁻² of different materials. (C) Tafel slope plots of the respective materials. (D) Nyquist plot of different materials. (E) Plots of scan rate dependent current densities for different materials. (F) Chronopotentiometric stability study for HER of NiNCs-1T-Mn-VTe₂ NS and Pt/C at current density of 50 mA cm⁻².

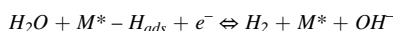
other mentioned as-synthesized catalysts, and the value is close to the commercially available Pt/C catalyst, indicating the superior potential of the NiNCs-1T-Mn-VTe₂ NS catalyst for HER catalysis. Moreover, as mentioned in the introduction section Mn has the best capacity to enhance the catalytic efficacy when doped in 1T-VTe₂ compared to the other transition metals such as Fe or Cr, as Mn can act as a strong electron donor to the host phase. To ascertain that we have measured the LSV for HER of Cr-VTe₂ and Fe-VTe₂. LSV curves after IR-correction is plotted in Fig. S11A. The results showed that Cr-VTe₂ and Fe-VTe₂ required overpotentials (η_{HER}) of (238, and 203) mV to reach the current density of 10 mA cm⁻², and (346, and 335) mV to reach the current density of 50 mA cm⁻², respectively, which are much higher compared to those of 1T-Mn-VTe₂ indicating superior function Mn dopant than Cr or Fe dopant for improving HER catalytic efficacy of 1T-VTe₂ [5,31–34,42]. Tafel plot analysis (Fig. 3C) was carried out to understand the kinetics involved in the catalytic reaction. The catalysts NiNCs-1T-Mn-VTe₂ NS, 1T-Mn-VTe₂, Mn-VTe₂ (1:3), Mn-VTe₂ (1:1), 1T-VTe₂, and Pt/C showed Tafel slope values of (71.5, 78.5, 89.1, 99.3, 133.2, and 55.3) mV dec⁻¹, respectively, indicating that the intercalation of the Mn and hybridization of the NiNCs with 1T-VTe₂ significantly accelerate the relatively sluggish HER kinetics of the VTe₂ catalyst.

The Tafel slope value specifies that the catalyst NiNCs-1T-Mn-VTe₂ NS followed the Volmer-Heyrovsky reaction mechanism for HER [5, 31–34,42]. The reaction is processed in two distinct stages, as follows:

The Volmer step:



The Heyrovsky step:



For the other control of the as-synthesized materials, the slope value is much higher, and the reaction is processed in a single Volmer rate-determining step for them, thus, cannot completely eliminate the sluggishness of the HER reaction. The above results established NiNCs-1T-Mn-VTe₂ NS as a superior and advanced catalyst for HER [5, 31–34,42]. Measurements of the Electrochemical Impedance Spectroscopy (EIS) were carried out to further authenticate the synergy with the η_{HER} and Tafel slope data (Fig. 3D). The results showed that the charge-transfer resistance (R_{ct}) of the catalysts follows the order Pt/C < NiNCs-1T-Mn-VTe₂ NS < 1T-Mn-VTe₂ < Mn-VTe₂ (1:3) < Mn-VTe₂ (1:1) < 1T-VTe₂ (Fig. 3D). The lowest charge transfer resistance was observed for NiNCs-1T-Mn-VTe₂ among all the as synthesized materials, which indicated the fastest charge transfer reaction for this in the electrode-electrolyte interface, hence establishing it as a superior catalyst for HER [5,31–34,42,49]. The performance of all the catalysts was further corroborated by electrochemically active surface area (ECSA) measurements. The ECSA values could be measured using the equation $\text{ECSA} = C_{\text{dl}}/C_s$, where C_s = the specific capacitance, and C_{dl} = the electrochemical double-layer capacitance of the flat surface. From the above equation, it can be seen that the electrochemically active surface area is directly proportional to the electrochemical double-layer capacitance (Fig. 3E, and Fig. S12, Supporting information). The electrochemical double-layer capacitance is found to be highest for the NiNCs-1T-Mn-VTe₂ NS (11.45 mF cm⁻²) among all the as synthesized materials. 1T-Mn-VTe₂, Mn-VTe₂ (1:3), Mn-VTe₂ (1:1), and 1T-VTe₂ showed C_{dl} values of (8.6, 5.85, 4.0, and 1.8) mF cm⁻², respectively (Fig. 3E, and Fig. S12, Supporting information). Pt/C has a C_{dl} values of (16.5) mF cm⁻² (Fig. 3E, and Fig. S12F, Supporting information). Thus, the interpretation of ECSA resembled the other electrochemical results, and established NiNCs-1T-Mn-VTe₂ NS as the superior catalyst [5, 31–34,42]. The long-term stability of the NiNCs-1T-Mn-VTe₂ NS was tested using chronopotentiometry stability test at the fixed current of 50 mA cm⁻² for 50 h and the potential showed only 4.5% degradation of the starting potential, whereas commercial Pt/C catalyst showed a 19%

degradation of the starting potential in the similar sets of condition (Fig. 3F), confirming the robust stability of the material. LSV data obtained after the chronopotentiometric stability test, and after 1000 consecutive LSV measurements, also confirm the robust stability of the materials (Fig. S13, Supporting information) [5,31–34,42]. The efficacy of the present material towards HER is compared with the contemporarily reported catalysts; the result is either superior or equivalent to the other contemporary reports (Table S2, Supporting information).

The catalytic efficiency of all the materials towards the oxygen evolution reaction (OER) was carried out, and Fig. 4 plots the obtained results. The LSV measurements were carried out at a fixed scan rate of 2 mV s⁻¹ for all the samples. The overpotentials for OER (η_{OER}) were obtained using the equation $\eta_{\text{OER}} = E_{\text{RHE}} - 1.23 \text{ V}$ [5,31–34,42]. The results showed that NiNCs-1T-Mn-VTe₂ NS, 1T-Mn-VTe₂, Mn-VTe₂ (1:3), Mn-VTe₂ (1:1), 1T-VTe₂, and RuO₂ required overpotentials (η_{OER}) of (258, 303, 318, 329, 351, and 287) mV to reach the current density of 40 mA cm⁻² (Fig. 4A & B). The other control materials NiNCs-1T-VTe₂, Mn-VTe₂(4:1), NiNCs-Mn-VTe₂(1:1), and NiNCs-1T-VTe₂ (1:3) required overpotentials (η_{OER}) of (387, 362, 331, and 320) mV to reach the current density of 40 mA cm⁻² (Fig. S11B, Supporting information). The overpotential values, as mentioned above, showed that the doping and intercalation of Mn and hybridization of NiNCs with VTe₂ have significantly and synergistically improved the OER catalytic performance; the required overpotential is even lower than the commercially-used RuO₂ catalyst [5,31–34,42]. To further discover the effect of the other transition metal doping in improving the catalytic performance of 1T-VTe₂, the LSV for OER of Cr-VTe₂ and Fe-VTe₂ was measured and the IR-corrected LSV results were plotted in Fig. S11B. The results showed that Cr-VTe₂ and Fe-VTe₂ required overpotentials (η_{OER}) of (445, and 398) mV to reach the current density of 40 mA cm⁻². The η_{OER} of Cr-VTe₂ and Fe-VTe₂ are much higher compared to the η_{OER} of 1T-Mn-VTe₂ indicating superior nature of Mn doping for improving the OER catalytic efficacy than Cr and Fe doping [5,31–34,42]. For the calculation of the η_{OER} , the current density of 40 mA cm⁻² was chosen to avoid the influence of the redox oxidation peak of the catalysts [5, 31–34,42]. The redox oxidation peak for the all the samples was observed between 1.24 V and 1.41 V (Fig. 4A, Fig. S11B, Supporting information) because of the $\text{V}^{4+}/\text{V}^{5+}$, $\text{Mn}^{2+}/\text{Mn}^{3+}$, and $\text{Ni}^{2+}/\text{Ni}^{3+}$ redox couples or by their overlaps depending upon the sample [5,12,42,53,54]. The intensity of the redox oxidation peak was lowest in 1T-VTe₂ and gradually increase to achieve highest value in NiNCs-1T-Mn-VTe₂ NS. Redox oxidation peak intensity regarding $\text{V}^{4+}/\text{V}^{5+}$ redox couples in the same potential region for VTe₂ is little low for OER and is similar to previous reports [12]. Introduction of Mn to VTe₂ showed significant increase in the redox oxidation peak intensity possibly due to presence of strong $\text{Mn}^{2+}/\text{Mn}^{3+}$ redox couples in that potential region and its overlapping with the $\text{V}^{4+}/\text{V}^{5+}$ redox couples [5,12,42,53,54]. Whereas, an increase in Mn concentration showed slight increase in the peak intensity of the redox oxidation peak from Mn-VTe₂ (4:1), to Mn-VTe₂ (1:1) to Mn-VTe₂ (1:3) (Fig. 4A, Fig. S11B, Supporting information). The adoption of the 1T-phase showed a very significant increase in intensity of the from Mn-VTe₂ (1:3) to 1T-Mn-VTe₂ possibly due to occurrence of the fast charge transfer reaction in the electrode-electrolyte interface associated with the increase in the internal conductivity of the material due to adoption of the 1T-phase [5,12,42,53,54]. The intensity of the redox oxidation peak was further increased from 1T-Mn-VTe₂ to NiNCs-1T-Mn-VTe₂ NS due to presence of strong $\text{Ni}^{2+}/\text{Ni}^{3+}$ redox couples in that potential region and its overlapping with the $\text{V}^{4+}/\text{V}^{5+}$, $\text{Mn}^{2+}/\text{Mn}^{3+}$ redox couples (Fig. 4A, Fig. S11B, Supporting information) [5,12,42,53,54]. The OER kinetics of the different materials was assessed by Tafel slope investigation (Fig. 4C). The Tafel slopes for NiNCs-1T-Mn-VTe₂ NS, 1T-Mn-VTe₂, Mn-VTe₂ (1:3), Mn-VTe₂ (1:1), 1T-VTe₂, and RuO₂ were found to be (48.8, 73.8, 80.4, 88.9, 120.1, and 55.1) mV dec⁻¹, respectively (Fig. 4C).

Among all the as-synthesized materials, the Tafel slope is lowest for NiNCs-1T-Mn-VTe₂ NS; moreover, the value is lower compared to the

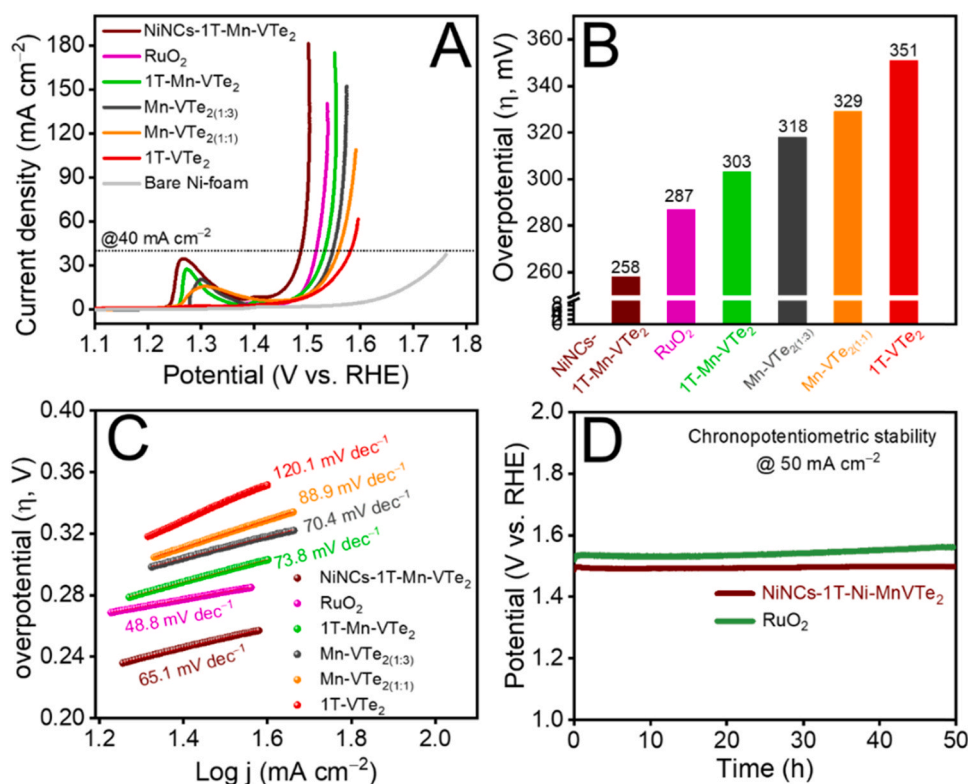


Fig. 4. (A) Linear sweep voltammetry (LSV) measurements curves for the oxygen evolution reaction (OER) of different materials. (B) Overpotential comparison (OER) of the materials at current densities of 40 mA cm². (C) Tafel slope plots of the respective materials. (D) Chronopotentiometric stability study for the OER of NiNCs-1T-Mn-VTe₂ NS and RuO₂.

commercially used OER catalyst RuO₂, indicating the superior nature of the NiNCs-1T-Mn-VTe₂ NS for efficient OER [5,31–34,42]. The lower charge-transfer resistance (R_{ct}) value and higher electrochemically active surface area (ECSA) of the NiNCs-1T-Mn-VTe₂ NS, as discussed above, also indicates the superior catalytic nature and possibility of the fast charge transfer reaction in the electrode electrolyte surface for OER (Fig. 3D & E, and Fig. S12, Supporting information) [5,31–34,42]. The reusability and the long-term stability of the NiNCs-1T-Mn-VTe₂ NS catalyst towards OER was tested using chronopotentiometry and consecutive LSV measurement (Fig. 4D, and Fig. S14, Supporting information). The results showed that after 50 h, only 2.8% degradation of the initial overpotential was observed in the chronopotentiometric stability test, whereas commercial RuO₂ catalyst showed a 5.6% degradation of the initial overpotential (Fig. 4C). After 1000 consecutive LSV measurements also, the LSV curve does not deviate significantly, indicating the superior stability of the catalyst for OER (Fig. S14, Supporting information) [5,31–34,42]. The efficacy of this catalyst towards OER is also compared with the recently reported catalysts, where the result is found to be superior to, or comparable with, the other recent reports (Table S3, Supporting information).

3.4. Overall water splitting study

The results obtained from the three-electrode system-based HER and OER showed that the NiNCs-1T-Mn-VTe₂ NS can function both as cathode and anode for superior overall water-splitting. The assumption was validated following LSV measurements using the NiNCs-1T-Mn-VTe₂ NS as both cathode and anode electrode. The control experiment was also performed using Pt/C coated Ni-foam as cathode, and RuO₂ coated Ni-foam as anode. The 1 M KOH solution was used as electrolyte for all the experiments. The results showed that the NiNCs-1T-Mn-VTe₂ NS (+/-) device has excellent water splitting performance with extremely low cell potential of 1.51 V at current density

10 mA cm⁻², and 1.63 V at current density 100 mA cm⁻² (Fig. 5A) [5, 31–34,42]. The control experiment showed that the RuO₂ (+) // Pt-C (-) device has the overall water splitting cell potential of 1.53 V at current density 10 mA cm⁻², and 1.76 V at current density 100 mA cm⁻² (Fig. 5A). Thus, the overall water splitting capacity of the NiNCs-1T-Mn-VTe₂ NS (+/-) device is identical to that of the commercially-used RuO₂ (+) // Pt-C (-) catalyst at lower current density; however, it showed better efficiency at relatively higher current density, establishing NiNCs-1T-Mn-VTe₂ NS as a highly potent catalyst for ultra-low potential overall water splitting [5,31–34,42]. The digital photograph of the NiNCs-1T-Mn-VTe₂ NS (+/-) device evidently confirms the formation of the O₂ and H₂ gas bubbles on the surface of the electrode surface (Fig. 5B). Faradaic efficiency (FE) was also measured using a lab-made water splitting device, where, NiNCs-1T-Mn-VTe₂ NS was used as both cathode and anode in a proportioned two-electrode arrangement. The anode and the cathode chambers were separated by a Nafion membrane (Fig. S15) [34,55]. Chronopotentiometry was then performed at current of 50 mA cm⁻² for a duration of 6 h and the produced volume of H₂ and O₂ gases was measured by measuring the amount of displaced water. Actual H₂ and O₂ gas production during this process was then used to calculate the Faradaic efficiency (FE) using equation-5. The FE was found to be around 97.1% for H₂ and 97.5% for O₂ in the present case [34,55]. Long-term chronoamperometric stability test of the NiNCs-1T-Mn-VTe₂ NS (+/-) and RuO₂ (+)/Pt-C (-) devices was carried out at steady state potential of 1.51 V (Fig. 5C). The results showed only 6.2% degradation of the initial current density for NiNCs-1T-Mn-VTe₂ NS (+/-) and 14.4% degradation of the initial current density for RuO₂ (+)/Pt-C (-) after 50 h [5,31–34,42]. Moreover, the stability test was also carried out following consecutive LSV measurements. The results showed that after 1000 consecutive measurements, the LSV curve does not change significantly (Fig. S16, Supporting information) [5,31–34,42]. The stability experiments established NiNCs-1T-Mn-VTe₂ NS (+/-) as a robust catalyst for overall

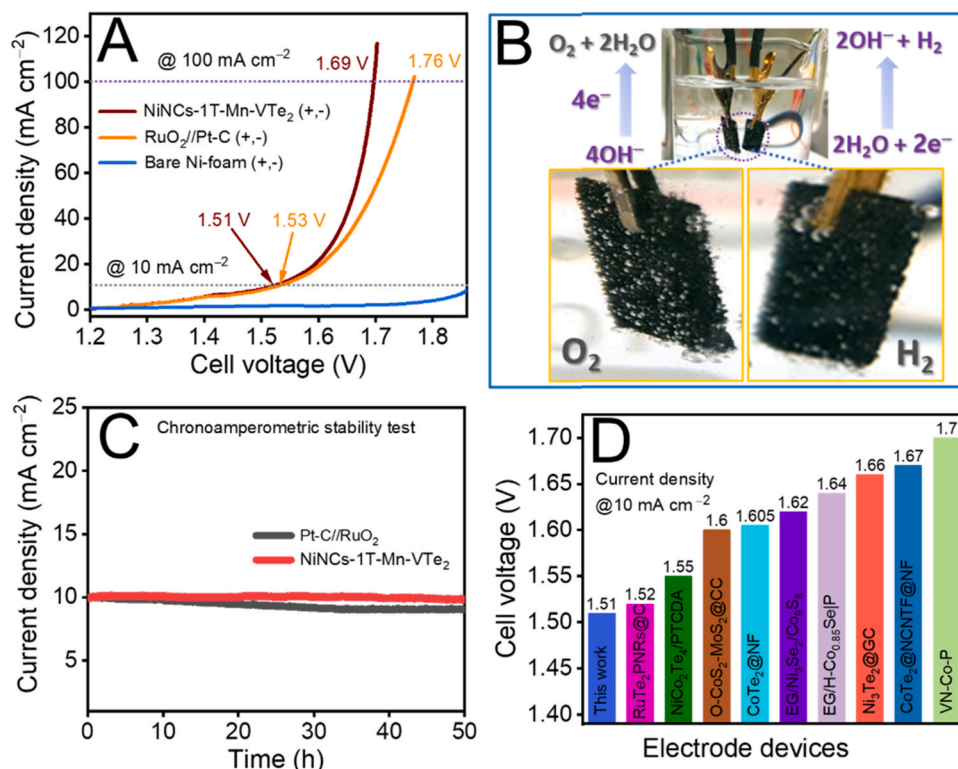


Fig. 5. (A) Linear sweep voltammetry (LSV) measurements curves of NiNCs-1T-Mn-VTe₂ (+/-), RuO₂ (+)//Pt-C (-), bare Ni-foam (+/-). (B) Digital image of the NiNCs-1T-Mn-VTe₂ (+/-) device during the electro-catalytic water splitting reaction showing the appearance of H₂ and O₂ gas bubbles on the surface of the cathode and anode. (C) Chronoamperometric stability test of the NiNCs-1T-Mn-VTe₂ (+/-) and RuO₂ (+)//Pt-C (-) device for 50 h. (D) Comparison of cell potential for the water splitting of NiNCs-1T-Mn-VTe₂ (+/-) devices with other recently reported materials [50–52,56–64].

water splitting. Comparison of the NiNCs-1T-Mn-VTe₂ NS (+/-) device result for overall water-splitting with that of the many recently reported transition metals-based electrocatalysts further established the superior nature of the present catalyst in comparison to the others (Fig. 5D, Table S4, Supporting information). Finally, to further assess the robustness of the NiNCs-1T-Mn-VTe₂ NS catalyst chronoamperometric post-stability test, FESEM and TEM images were obtained (Fig. 6A & B). The results showed no significant changes in the morphology of the catalyst after the stability test. Moreover, the presence of NiNCs was also

visible in the TEM images (Fig. 6B); some of them are marked in circles. The elemental mapping of the NiNCs-1T-Mn-VTe₂ NS post-stability test was also taken (Fig. 6C), and the results showed no significant changes in the elemental composition post-stability test, which establishes the robustness of the NiNCs-1T-Mn-VTe₂ NS catalyst [5,31–34,42]. The XPS results of the NiNCs-1T-Mn-VTe₂ was also obtained after the chronopotentiometric stability test (Fig. S17, Supporting information). The results regarding vanadium (2p) (Fig. S17A, Supporting information) showed peaks at 524.2 eV, 522.7 eV, 516.8 eV and 516.1 eV

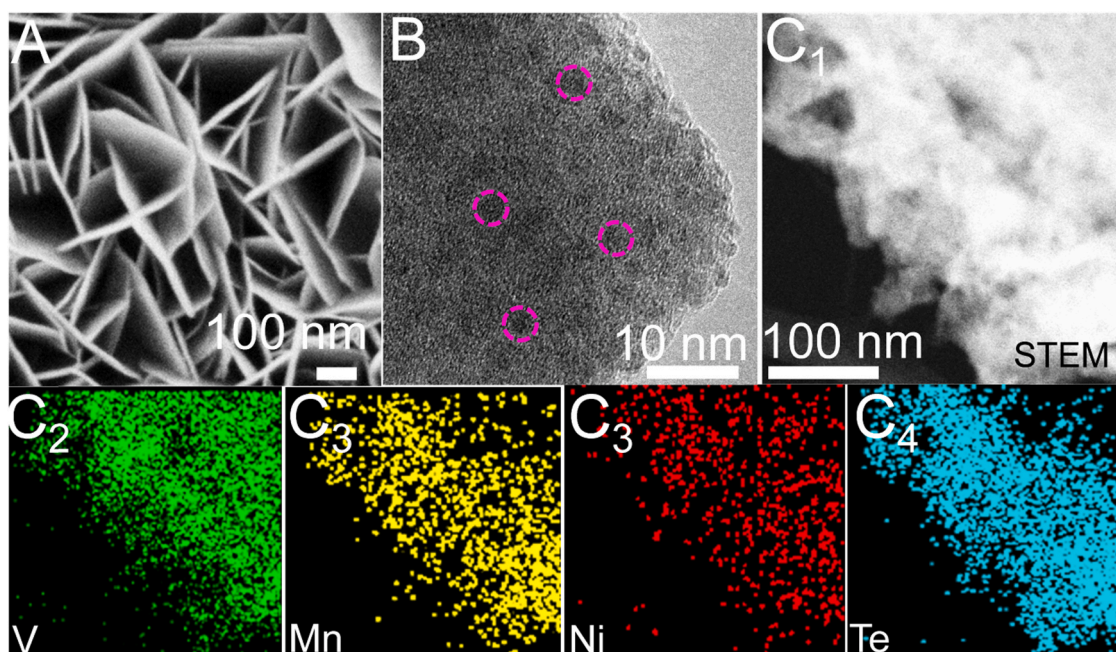


Fig. 6. (A) FESEM image, (B) TEM image, and (C₁) & (C₂)–(C₄) STEM images corresponding to the elemental mapping after the stability test of NiNCs-1T-Mn-VTe₂.

corresponding to $V^{5+} 2p_{1/2}$, $V^{4+} 2p_{1/2}$, $V^{5+} 2p_{3/2}$ and $V^{4+} 2p_{3/2}$ respectively [11,12,20,38]. The Te 3d (Fig. S17B, Supporting information) showed the presence of peaks at 586.5 eV, 576.1 eV 583.5 eV, 573.2 eV corresponding to $TeO_2 (3d_{3/2})$ and $TeO_2 (3d_{5/2})$, Te-metallic ($3d_{3/2}$) and Te-metallic ($3d_{5/2}$), respectively [10–13,43]. The Mn 2p showed peaks at 655.9 eV, 653.5 eV, 652.0 eV, 646.7 eV, 642.9 eV, and 641.1 eV (Fig. S17C, Supporting information) corresponding to $Mn^{4+} 2p_{1/2}$, $Mn^{3+} 2p_{1/2}$, $Mn^{2+} 2p_{1/2}$, $Mn^{4+} 2p_{3/2}$, $Mn^{3+} 2p_{3/2}$ and $Mn^{2+} 2p_{3/2}$ respectively [7,14]. The Ni 2p (Fig. S17D, Supporting information) showed peaks at 870.5 eV, 868.5 eV, 852.9 eV, and 851.4 eV corresponding to $Ni^{2+} 2p_{1/2}$, Ni (metal) $2p_{1/2}$, $Ni^{2+} 2p_{3/2}$, and Ni (metal) $2p_{3/2}$ respectively [5, 16,19]. The results showed no significant changes in the peak position compared to the as-synthesized NiNCs–1T–Mn–VTe₂ also confirm robust stability. However, the intensity regarding Te-metallic peaks decreases whereas intensity regarding peak TeO_2 correspondingly increases which may be due to the superficial oxidation of the Te species during the electrocatalytic reaction (Fig. 2D, S17B, Supporting information) [10–13,43]. The peak regarding Ni (metal) though, does not significantly changed to that of Ni^{2+} in intensity or position compared to the as-synthesized NiNCs–1T–Mn–VTe₂ (Fig. 2F, S17D, Supporting information), indicating no significant change in the metallic nature of the NiNCs during the electrocatalytic reaction [5,31–34,42].

4. Conclusion

In summary, we have demonstrated the fabrication of a highly efficient catalyst following the hybridization of NiNCs with Mn intercalated and doped metallic (1T) vanadium telluride nanosheet (NiNCs–1T–Mn–VTe₂ NS) for ultra-low potential overall water splitting. Intercalation and doping of Mn in 1T–VTe₂ helps in further stabilization of the 1T-phase and the development of proper nanosheet structure with high surface area and porosity. These have significantly helped improve both the HER and OER performance. NiNCs is also a superior catalyst for water splitting, while hybridization of NiNCs with 1T–Mn–VTe₂ helps in further improvement in the HER and OER performance, and establishes NiNCs–1T–Mn–VTe₂ NS as a true catalyst for ultra-low potential overall water splitting. NiNCs–1T–Mn–VTe₂ NS showed it only required overpotentials of (61 and 137) mV to reach the current density of (10 and 50) mA cm^{−2}, respectively, for HER, and overpotential of 258 mV to reach the current density of 40 mA cm^{−2} for OER. Moreover, the NiNCs–1T–Mn–VTe₂ NS (+,−) device required a cell potential of 1.51 V at a current density 10 mA cm^{−2}, and 1.63 V at a current density of 100 mA cm^{−2}, for overall water splitting. The Faradaic efficiency was found to be around 97.1% for H₂ and 97.5% for O₂ in the present case. Moreover, NiNCs–1T–Mn–VTe₂ showed robust stability for repetitive use as catalyst. Therefore, we can conclude that the novel approach established in the present work following strategic hybridization of an active metal nanocluster with binary metal chalcogenide could be an ideal direction for developing efficient electrocatalysts based on earth-abundant materials for solving industrial-scale green H₂ production challenges.

CRediT authorship contribution statement

Uday Narayan Pan: Methodology, Investigation, Validation, Formal analysis. **Dasu Ram Paudel:** Methodology, Data curation, Writing – original draft. Visualization. **Amit Kumar Das:** Methodology, Data curation, Visualization. **Thangjam Ibomcha Singh:** Methodology, Data curation, Visualization. **Nam Hoon Kim:** Conceptualization, Writing – review & editing, supervision. **Joong Hee Lee:** Conceptualization, Writing – review & editing, Supervision, Project administration.

Declaration of Competing Interest

The authors declare that they have no known competing financial interests or personal relationships that could have appeared to influence

the work reported in this paper.

Acknowledgements

This research was supported by the Basic Science Research Program (2017R1A2B3004917) through the National Research Foundation funded by the Ministry of Science and ICT, Republic of Korea. The authors also thank Mr. Chandan Chandru Gudal, Dr. Jayaraman Balamurugan, Prof. Duy Thanh Tran, and Mr. Huu Tuan Le, for their help.

Appendix A. Supporting information

Supplementary data associated with this article can be found in the online version at doi:10.1016/j.apcatb.2021.120780.

References

- [1] I. Dincer, C. Zamfirescu, Sustainable hydrogen production, *Sustain. Hydrog. Prod.* 305 (2016) 1–479, <https://doi.org/10.1016/b978-0-444-64203-5.00001-0>.
- [2] Z.W. Seh, J. Kibsgaard, C.F. Dickens, I. Chorkendorff, J.K. Nørskov, T.F. Jaramillo, Combining theory and experiment in electrocatalysis: Insights into materials design, *Science* 355 (2017), ead4998, <https://doi.org/10.1126/science.ad4998>.
- [3] S. Chu, A. Majumdar, Opportunities and challenges for a sustainable energy future, *Nature* 488 (2012) 294–303, <https://doi.org/10.1038/nature11475>.
- [4] M.S. Dresselhaus, I.L. Thomas, Alternative energy technologies, *Dresselhaus2001*, *Nature* 414 (2001) 332–337, <https://doi.org/10.1038/35104599>.
- [5] U.N. Pan, T.I. Singh, D.R. Paudel, C.C. Gudal, N.H. Kim, J.H. Lee, Covalent doping of Ni and P on 1T-enriched MoS₂ bifunctional 2D-nanostructures with active basal planes and expanded interlayers boosts electrocatalytic water splitting, *J. Mater. Chem. A* 8 (2020) 19654–19664, <https://doi.org/10.1039/d0ta05865c>.
- [6] D.R. Paudel, U.N. Pan, T.I. Singh, C.C. Gudal, N.H. Kim, J.H. Lee, Fe and P doped 1T-phase enriched WS₂ 3D-dendritic nanostructures for efficient overall water splitting, *Appl. Catal. B: Environ.* 286 (2021), 119897, <https://doi.org/10.1016/j.apcatb.2021.119897>.
- [7] U.N. Pan, V. Sharma, T. Kshetri, T.I. Singh, D.R. Paudel, N.H. Kim, J.H. Lee, Freestanding 1T-Mn_xMo_{1-x}S₂-ySe_y and MoFe₂S₄-zSe_z ultrathin nanosheet-structured electrodes for highly efficient flexible solid-state asymmetric supercapacitors, *Small* 16 (2020) 4–15, <https://doi.org/10.1002/sml.202001691>.
- [8] Y.C. Lin, D.O. Dumcenco, Y.S. Huang, K. Suenaga, Atomic mechanism of the semiconducting-to-metallic phase transition in single-layered MoS₂, *Nat. Nanotechnol.* 9 (2014) 391–396, <https://doi.org/10.1038/nnano.2014.64>.
- [9] U.N. Pan, V. Sharma, T. Kshetri, T.I. Singh, D.R. Paudel, N.H. Kim, J.H. Lee, Freestanding 1T-Mn x Mo 1–x S 2–y Se y and MoFe 2 S 4–z Se z ultrathin nanosheet-structured electrodes for highly efficient flexible solid-state asymmetric supercapacitors, *Small* 16 (2020), 2001691, <https://doi.org/10.1002/sml.202001691>.
- [10] K. Leng, Z. Chen, X. Zhao, W. Tang, B. Tian, C.T. Nai, W. Zhou, K.P. Loh, Phase restructuring in transition metal dichalcogenides for highly stable energy storage, *ACS Nano* 10 (2016) 9208–9215, <https://doi.org/10.1021/acsnano.6b05746>.
- [11] J. Li, B. Zhao, P. Chen, R. Wu, B. Li, Q. Xia, G. Guo, J. Luo, K. Zang, Z. Zhang, H. Ma, G. Sun, X. Duan, X. Duan, Synthesis of ultrathin metallic MTe₂ (M = V, Nb, Ta) single-crystalline nanoplates, *Adv. Mater.* 30 (2018) 1–8, <https://doi.org/10.1002/adma.201801043>.
- [12] J. Shi, Y. Huan, X. Zhao, P. Yang, M. Hong, C. Xie, S. Pennycook, Y. Zhang, Two-dimensional metallic vanadium ditelluride as a high-performance electrode material, *ACS Nano* 15 (2021) 1858–1868, <https://doi.org/10.1021/acsnano.0c10250>.
- [13] D. Won, D.H. Kiem, H. Cho, D. Kim, Y. Kim, M.Y. Jeong, C. Seo, J. Kim, J. Park, M. J. Han, H. Yang, S. Cho, Polymorphic spin, charge, and lattice waves in vanadium ditelluride, *Adv. Mater.* 32 (2020), 1906578, <https://doi.org/10.1002/adma.201906578>.
- [14] K. Zhang, S. Feng, J. Wang, A. Azcatl, N. Lu, R. Addou, N. Wang, C. Zhou, J. Lerach, V. Bojan, M.J. Kim, L.Q. Chen, R.M. Wallace, M. Terrones, J. Zhu, J.A. Robinson, Manganese doping of monolayer MoS₂: The substrate is critical, *Nano Lett.* 15 (2015) 6586–6591, <https://doi.org/10.1021/acs.nanolett.5b02315>.
- [15] D. Jiang, W. Ma, R. Yang, B. Quan, D. Li, S. Meng, M. Chen, Nickel–manganese bimetallic phosphides porous nanosheet arrays as highly active bifunctional hydrogen and oxygen evolution electrocatalysts for overall water splitting, *Electrochim. Acta* 329 (2020), 135121, <https://doi.org/10.1016/j.electacta.2019.135121>.
- [16] K.S. Joya, L. Sinatra, L.G. AbdulHalim, C.P. Joshi, M.N. Hedhili, O.M. Bakr, I. Hussain, Atomically monodisperse nickel nanoclusters as highly active electrocatalysts for water oxidation, *Nanoscale* 8 (2016) 9695–9703, <https://doi.org/10.1039/C6NR00709K>.
- [17] U.N. Pan, R. Khandelia, P. Sanpui, S. Das, A. Paul, A. Chattopadhyay, Protein-based multifunctional nanocarriers for imaging, photothermal therapy, and anticancer drug delivery, *ACS Appl. Mater. Interfaces* 9 (2017) 19495–19501, <https://doi.org/10.1021/acsami.6b06099>.
- [18] T. Kawawaki, A. Ebina, Y. Hosokawa, S. Ozaki, D. Suzuki, S. Hossain, Y. Negishi, Thiolate-protected metal nanoclusters: recent development in synthesis,

- understanding of reaction, and application in energy and environmental field, *Small* 17 (2021), 2005328, <https://doi.org/10.1002/sml.202005328>.
- [19] Z. Zhang, J. Su, A.S. Matias, M. Gordon, Y.-S. Liu, J. Guo, C. Song, C. Dun, D. Prendergast, G.A. Somorjai, J.J. Urban, Enhanced and stabilized hydrogen production from methanol by ultrasmall Ni nanoclusters immobilized on defect-rich h-BN nanosheets, *Proc. Natl. Acad. Sci. U.S.A.* 117 (2020) 29442–29452, <https://doi.org/10.1073/pnas.2015897117>.
 - [20] P.K.J. Wong, W. Zhang, J. Zhou, F. Bussolotti, X. Yin, L. Zhang, A.T. N'Diaye, S. A. Morton, W. Chen, J. Goh, M.P. de Jong, Y.P. Feng, A.T.S. Wee, Metallic 1T phase, 3d 1 electronic configuration and charge density wave order in molecular beam epitaxy grown monolayer vanadium ditelluride, *ACS Nano* 13 (2019) 12894–12900, <https://doi.org/10.1021/acsnano.9b05349>.
 - [21] S. Synthesis E. Properties M. Au Size-Focus. Synth., Opt. 3 2009 3795 3803.
 - [22] U.N. Pan, P. Sanpui, A. Paul, A. Chattopadhyay, Protein-nanoparticle agglomerates as a plasmonic magneto-luminescent multifunctional nanocarrier for imaging and combination therapy, *ACS Appl. Bio Mater.* 2 (2019) 3144–3152, <https://doi.org/10.1021/acsbam.9b00210>.
 - [23] J. Balamurugan, T.T. Nguyen, V. Aravindan, N.H. Kim, S.H. Lee, J.H. Lee, All ternary metal selenide nanostructures for high energy flexible charge storage devices, *Nano Energy* 65 (2019), 103999, <https://doi.org/10.1016/j.nanoen.2019.103999>.
 - [24] C. Li, J. Balamurugan, N.H. Kim, J.H. Lee, Hierarchical Zn–Co–S nanowires as advanced electrodes for all solid state asymmetric supercapacitors, *Adv. Energy Mater.* 8 (2018) 1–12, <https://doi.org/10.1002/aenm.201702014>.
 - [25] Y. Li, X. Tan, H. Tan, H. Ren, S. Chen, W. Yang, S.C. Smith, C. Zhao, Phosphine vapor-assisted construction of heterostructured Ni₂P/NiTe₂ catalysts for efficient hydrogen evolution, *Energy Environ. Sci.* 13 (2020) 1799–1807, <https://doi.org/10.1039/d0ee00666a>.
 - [26] L. Hu, X. Zeng, X. Wei, H. Wang, Y. Wu, W. Gu, L. Shi, C. Zhu, Interface engineering for enhancing electrocatalytic oxygen evolution of NiFe LDH/NiTe heterostructures, *Appl. Catal. B Environ.* 273 (2020) 1–7, <https://doi.org/10.1016/j.apcatb.2020.119014>.
 - [27] J. Balamurugan, T.T. Nguyen, V. Aravindan, N.H. Kim, J.H. Lee, Flexible solid-state asymmetric supercapacitors based on nitrogen-doped graphene encapsulated ternary metal-nitrides with ultralong cycle life, *Adv. Funct. Mater.* 28 (2018) 1–17, <https://doi.org/10.1002/adfm.201804663>.
 - [28] X. Yu, Y. Kang, S. Wang, K.S. Hui, K.N. Hui, H. Zhao, J. Li, B. Li, J. Xu, L. Chen, H. Shao, Integrating PtNi nanoparticles on NiFe layered double hydroxide nanosheets as a bifunctional catalyst for hybrid sodium-air batteries, *J. Mater. Chem. A* 8 (2020) 16355–16365, <https://doi.org/10.1039/d0ta04602g>.
 - [29] B. Ramulu, S. Chandra Sekhar, S.J. Arbaz, J.S. Yu, Nano-Ag laminated ternary layered double hydroxides for hybrid supercapacitors, *Chem. Eng. J.* 420 (2021), 130376, <https://doi.org/10.1016/j.cej.2021.130376>.
 - [30] F. Mingli, L. Xue, W. Dandan, W. Yinling, L. Maoguo, Fabrication of Te@NiTe₂/NiS heterostructures for electrocatalytic hydrogen evolution reaction, *Electrochim. Acta* 328 (2019), 135075, <https://doi.org/10.1016/j.electacta.2019.135075>.
 - [31] V.H. Hoa, D.T. Tran, S. Prabhakaran, D.H. Kim, N. Hameed, H. Wang, N.H. Kim, J. H. Lee, Ruthenium single atoms implanted continuous MoS₂/Mo₂C heterostructure for high-performance and stable water splitting, *Nano Energy* 88 (2021), 106277, <https://doi.org/10.1016/j.nanoen.2021.106277>.
 - [32] D. Van Dao, T.T.D. Nguyen, P. Uthirakumar, Y.H. Cho, G.C. Kim, J.K. Yang, D. T. Tran, T.D. Le, H. Choi, H.Y. Kim, Y.T. Yu, I.H. Lee, Insightful understanding of hot-carrier generation and transfer in plasmonic Au@CeO₂ core-shell photocatalysts for light-driven hydrogen evolution improvement, *Appl. Catal. B: Environ.* 286 (2021), 119947, <https://doi.org/10.1016/j.apcatb.2021.119947>.
 - [33] D.C. Nguyen, D.T. Tran, T.L.L. Doan, D.H. Kim, N.H. Kim, J.H. Lee, Rational design of core@shell structured CoSx@Cu₂MoS₄ hybridized MoS₂/N,S-codoped graphene as advanced electrocatalyst for water splitting and Zn-Air battery, *Adv. Energy Mater.* 10 (2020) 1–14, <https://doi.org/10.1002/aenm.201903289>.
 - [34] D.T. Tran, V.H. Hoa, S. Prabhakaran, D.H. Kim, N.H. Kim, J.H. Lee, Activated CuNi@Ni Core@shell structures via oxygen and nitrogen dual coordination assembled on 3D CNTs-graphene hybrid for high-performance water splitting, *Appl. Catal. B: Environ.* 294 (2021), 120263, <https://doi.org/10.1016/j.apcatb.2021.120263>.
 - [35] V.H. Hoa, D.T. Tran, D.C. Nguyen, D.H. Kim, N.H. Kim, J.H. Lee, Molybdenum and phosphorus dual doping in cobalt monolayer interfacial assembled cobalt nanowires for efficient overall water splitting, *Adv. Funct. Mater.* 30 (2020) 1–12, <https://doi.org/10.1002/adfm.202002533>.
 - [36] C. Li, Q. Li, Y.V. Kaneti, D. Hou, Y. Yamauchi, Y. Mai, Self-assembly of block copolymers towards mesoporous materials for energy storage and conversion systems, *Chem. Soc. Rev.* 49 (2020) 4681–4736, <https://doi.org/10.1039/d0cs00021c>.
 - [37] J. Balamurugan, C. Li, V. Aravindan, N.H. Kim, J.H. Lee, Hierarchical Ni-Mo-S and Ni-Fe-S nanosheets with ultrahigh energy density for flexible all solid-state supercapacitors, *Adv. Funct. Mater.* 28 (2018) 1–14, <https://doi.org/10.1002/adfm.201803287>.
 - [38] K.D. Bronsema, G.W. Bus, G.A. Wiegiers, The crystal structure of vanadium ditelluride, V_{1+x}Te₂, *J. Solid State Chem.* 53 (1984) 415–421, [https://doi.org/10.1016/0022-4596\(84\)90120-8](https://doi.org/10.1016/0022-4596(84)90120-8).
 - [39] C.F. Holder, R.E. Schaak, Tutorial on powder X-ray diffraction for characterizing nanoscale materials, *ACS Nano* 13 (2019) 7359–7365, <https://doi.org/10.1021/acsnano.9b05157>.
 - [40] A. Gili, L. Schlicker, M.F. Bekheet, O. Görke, D. Kober, U. Simon, P. Littlewood, R. Schomäcker, A. Doran, D. Gaissmaier, T. Jacob, S. Selve, A. Gurlö, Revealing the mechanism of multiwalled carbon nanotube growth on supported nickel nanoparticles by in situ synchrotron X-ray diffraction, density functional theory, and molecular dynamics simulations, *ACS Catal.* 9 (2019) 6999–7011, <https://doi.org/10.1021/acscatal.9b00733>.
 - [41] T.T. Nguyen, J. Balamurugan, V. Aravindan, N.H. Kim, J.H. Lee, Boosting the energy density of flexible solid-state supercapacitors via both ternary NiV₂Se₄ and NiFe₂Se₄ nanosheet arrays, *Chem. Mater.* 31 (2019) 4490–4504, <https://doi.org/10.1021/acs.chemmater.9b01101>.
 - [42] J. Balamurugan, T.T. Nguyen, D.H. Kim, N.H. Kim, J.H. Lee, 3D nickel molybdenum oxyselenide (Ni_{1-x}MoxOSe) nanoarchitectures as advanced multifunctional catalyst for Zn-air batteries and water splitting, *Appl. Catal. B: Environ.* 286 (2021), 119909, <https://doi.org/10.1016/j.apcatb.2021.119909>.
 - [43] U. De Silva, J. Masud, N. Zhang, Y. Hong, W.P.R. Liyanage, M. Asle Zaem, M. Nath, Nickel telluride as a bifunctional electrocatalyst for efficient water splitting in alkaline medium, *J. Mater. Chem. A* 6 (2018) 7608–7622, <https://doi.org/10.1039/c8ta01760c>.
 - [44] Z. Zhang, W. Hu, S. Xiao, Shell and subshell periodic structures of icosahedral nickel nanoclusters, *J. Chem. Phys.* 122 (2005), 214501, <https://doi.org/10.1063/1.1925278>.
 - [45] H. Li, L. Li, A. Pedersen, Y. Gao, N. Khetrapal, H. Jónsson, X.C. Zeng, Magic-number gold nanoclusters with diameters from 1 to 3.5 nm: relative stability and catalytic activity for CO oxidation, *Nano Lett.* 15 (2015) 682–688, <https://doi.org/10.1021/nl504192u>.
 - [46] Y. Chen, Z. Liu, J. Li, X. Cheng, J. Ma, H. Wang, D. Li, Robust interlayer coupling in two-dimensional perovskite/monolayer transition metal dichalcogenide heterostructures, *ACS Nano* 14 (2020) 10258–10264, <https://doi.org/10.1021/acsnano.0c03624>.
 - [47] E.M. Alexeev, A. Catanzaro, O.V. Skrypkina, P.K. Nayak, S. Ahn, S. Pak, J. Lee, J. I. Sohn, K.S. Novoselov, H.S. Shin, A.I. Tartakovskii, Imaging of interlayer coupling in van der Waals heterostructures using a bright-field optical microscope, *Nano Lett.* 17 (2017) 5342–5349, <https://doi.org/10.1021/acs.nanolett.7b01763>.
 - [48] H. Fang, C. Battaglia, C. Carraro, S. Nemsak, B. Ozdol, G.S. Kang, H.A. Bechtel, S. B. Desai, F. Kronast, A.A. Unal, G. Conti, C. Conlon, G.K. Palsson, M.C. Martin, A. M. Minor, C.S. Fadley, E. Yablonovitch, R. Maboudian, A. Javey, Strong interlayer coupling in van der Waals heterostructures built from single-layer chalcogenides, *Proc. Natl. Acad. Sci. U.S.A.* 111 (2014) 6198–6202, <https://doi.org/10.1073/pnas.1405435111>.
 - [49] V.H. Hoa, D.T. Tran, H.T. Le, N.H. Kim, J.H. Lee, Hierarchically porous nickel-cobalt phosphide nanoneedle arrays loaded micro-carbon spheres as an advanced electrocatalyst for overall water splitting application, *Appl. Catal. B: Environ.* 253 (2019) 235–245, <https://doi.org/10.1016/j.apcatb.2019.04.017>.
 - [50] P. Liu, J. Zhu, J. Zhang, P. Xi, K. Tao, D. Gao, D. Xue, P dopants triggered new basal plane active sites and enlarged interlayer spacing in mos₂ nanosheets toward electrocatalytic hydrogen evolution, *ACS Energy Lett.* 2 (2017) 745–752, <https://doi.org/10.1021/acsenenergylett.7b00111>.
 - [51] J. Xie, J. Zhang, S. Li, F. Grote, X. Zhang, H. Zhang, R. Wang, Y. Lei, B. Pan, Y. Xie, Controllable disorder engineering in oxygen-incorporated MoS₂ ultrathin nanosheets for efficient hydrogen evolution, *J. Am. Chem. Soc.* 135 (2013) 17881–17888, <https://doi.org/10.1021/ja408329q>.
 - [52] M.A. Lukowski, A.S. Daniel, F. Meng, A. Forticaux, L. Li, S. Jin, Enhanced hydrogen evolution catalysis from chemically exfoliated metallic MoS₂ nanosheets, *J. Am. Chem. Soc.* 135 (2013) 10274–10277, <https://doi.org/10.1021/ja404523s>.
 - [53] J. Zhu, L. Hu, P. Zhao, L.Y.S. Lee, K.Y. Wong, Recent advances in electrocatalytic hydrogen evolution using nanoparticles, *Chem. Rev.* 120 (2020) 851–918, <https://doi.org/10.1021/acs.chemrev.9b00248>.
 - [54] S. Anantharaj, S.R. Ede, K. Sakthikumar, K. Karthick, S. Mishra, S. Kundu, Recent trends and perspectives in electrochemical water splitting with an emphasis on sulfide, selenide, and phosphide catalysts of Fe, Co, and Ni: a review, *ACS Catal.* 6 (2016) 8069–8097, <https://doi.org/10.1021/acscatal.6b02479>.
 - [55] T.L.L. Doan, D.C. Nguyen, S. Prabhakaran, D.H. Kim, D.T. Tran, N.H. Kim, J.H. Lee, Single-atom Co-decorated MoS₂ nanosheets assembled on metal nitride nanorod arrays as an efficient bifunctional electrocatalyst for pH-universal water splitting, *Adv. Funct. Mater.* 31 (2021) 1–15, <https://doi.org/10.1002/adfm.202100233>.
 - [56] B. Sun, X. Wang, D. Yang, Y. Chen, Self-assembled Co_{0.85}Se/carbon nanowires as a highly effective and stable electrocatalyst for the hydrogen evolution reaction, *RSC Adv.* 9 (2019) 17238–17245, <https://doi.org/10.1039/c9ra02007a>.
 - [57] Y. Yin, J. Xu, W. Guo, Z. Wang, X. Du, C. Chen, Z. Zheng, D. Liu, D. Qu, Z. Xie, H. Tang, J. Li, A single-step fabrication of CoTe₂ nanofilms electrode toward efficient overall water splitting, *Electrochim. Acta* 307 (2019) 451–458, <https://doi.org/10.1016/j.electacta.2019.03.213>.
 - [58] P. Liu, J. Yan, J. Mao, J. Li, D. Liang, W. Song, In-plane intergrowth CoS₂/MoS₂ nanosheets: binary metal-organic framework evolution and efficient alkaline HER electrocatalysis, *J. Mater. Chem. A* 8 (2020) 11435–11441, <https://doi.org/10.1039/d0ta00897d>.
 - [59] B. Golrokh Amin, U. De Silva, J. Masud, M. Nath, Ultrasensitive and highly selective Ni₃Te₂ as a nonenzymatic glucose sensor at extremely low working potential, *ACS Omega* 4 (2019) 11152–11162, <https://doi.org/10.1021/acsomega.9b01063>.
 - [60] Y. Hou, M. Qiu, G. Nam, M.G. Kim, T. Zhang, K. Liu, X. Zhuang, J. Cho, C. Yuan, X. Feng, Integrated hierarchical cobalt sulfide/nickel selenide hybrid nanosheets as an efficient three-dimensional electrode for electrochemical and photoelectrochemical water splitting, *Nano Lett.* 17 (2017) 4202–4209, <https://doi.org/10.1021/acs.nanolett.7b01030>.
 - [61] X. Wang, X. Huang, W. Gao, Y. Tang, P. Jiang, K. Lan, R. Yang, B. Wang, R. Li, Metal-organic framework derived CoTe₂ encapsulated in nitrogen-doped carbon nanotube frameworks: a high-efficiency bifunctional electrocatalyst for overall water splitting, *J. Mater. Chem. A* 6 (2018) 3684–3691, <https://doi.org/10.1039/c7ta10728e>.

- [62] Y. Xiao, C. Tian, M. Tian, A. Wu, H. Yan, C. Chen, L. Wang, Y. Jiao, H. Fu, Cobalt-vanadium bimetal-based nanoplates for efficient overall water splitting, *Sci. China Mater.* 61 (2018) 80–90, <https://doi.org/10.1007/s40843-017-9113-1>.
- [63] L. Tao, M. Huang, S. Guo, Q. Wang, M. Li, X. Xiao, G. Cao, Y. Shao, Y. Shen, Y. Fu, M. Wang, Surface modification of NiCo_2Te_4 nanoclusters: a highly efficient electrocatalyst for overall water-splitting in neutral solution, *Appl. Catal. B Environ.* 254 (2019) 424–431, <https://doi.org/10.1016/j.apcatb.2019.05.010>.
- [64] J. Wang, L. Han, B. Huang, Q. Shao, H.L. Xin, X. Huang, Amorphization activated ruthenium-tellurium nanorods for efficient water splitting, *Nat. Commun.* 10 (2019) 1–11, <https://doi.org/10.1038/s41467-019-13519-1>.